Masters thesis

Thermodynamics of Solutes in Cementite Using First-Principles Calculations

Jang, Jae Hoon (張在勳)

Computational Metallurgy

Graduate Institute of Ferrous Technology

Pohang University of Science and Technology

2009

Thermodynamics of Solutes in Cementite Using First-Principles Calculations

2009

Jang, Jae Hoon

제일원리를 이용한 cementite내 고용원소 열역학 계산

Thermodynamics of Solutes in Cementite Using First-Principles Calculations

Thermodynamics of Solutes in Cementite Using First-Principles Calculations

By

Jang, Jae Hoon
Computational Metallurgy
Graduate Institute of Ferrous Technology
Pohang University of Science and Technology

A thesis submitted to the faculty of Pohang University of Science and Technology in partial fulfillments of the requirements for the degree of Master of Science in the Graduate Institute of Ferrous Technology (Computational Metallurgy)

Pohang, Korea
December 19th, 2008

Approved by

Prof. Bhadeshia, H. K. D. H.	Prof. Kim, In Gee
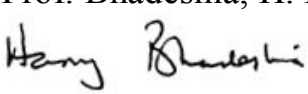	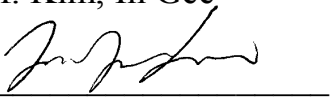
Major Advisor	Co-Advisor

Thermodynamics of Solutes in Cementite Using First-Principles Calculations

Jang, Jae Hoon

This dissertation is submitted for the degree of Master of Science at the Graduate Institute of Ferrous Technology of Pohang University of Science and Technology. The research reported herein was approved by the committee of Thesis Appraisal

December 19th, 2008

Thesis Review Committee
Chairman: Prof. Lee, Hae Geon
(Signature)_____
Member: Prof. Kim, In Gee
(Signature)_____
Member: Prof. Qin, Rong Shan
(Signature)_____

MFT 20072860 Jang, Jae Hoon
Thermodynamics of Solutes in Cementite
Using First-Principles Calculations,
Computational Metallurgy 2009
Adivisor: Prof. Bhadeshia, H.K.D.H.; Prof. Kim, In Gee
Text in English

Abstract

Cementite precipitation from austentite in steels can be suppressed by alloying with silicon and aluminum. There are, however, no validated thermodynamic data to enable phase equilibria to be estimated when silicon and aluminum are present in cementite. The formation energies of Fe_3C, $(Fe_{11}M^{4c}_{Fe})C_4$ and $(Fe_{11}M^{8d}_{Fe})C_4$, where M means an alloying element Si, Al or Mn, have therefore been estimated using first-principles calculations based on the total energy all-electron full-potential linearized augmented plane-wave method within the generalized gradient approximation to density functional theory. The ground state properties such as lattice constants and bulk moduli have also been calculated. The calculations show that $(Fe_{11}Si^{4c}_{Fe})C_4$ and $(Fe_{11}Si^{8d}_{Fe})C_4$ have about 52.1 kJ mol^{-1} and 37.2 kJ mol^{-1} greater formation energy, respectively, than Fe_3C, while $(Fe_{11}Al^{4c}_{Fe})C_4$, $(Fe_{11}Al^{8d}_{Fe})C_4$, $(Fe_{11}Mn^{4c}_{Fe})C_4$ and $(Fe_{11}Mn^{8d}_{Fe})C_4$ have about 10.0 kJ mol^{-1}, 13.6 kJ mol^{-1}, 4.4 kJ mol^{-1} and 5.0 kJ mol^{-1} smaller. The formation energy for hypothetical cementite Si_3C, Al_3C and Mn_3C have also been calculated to be about 256.4 kJ mol^{-1}, 95.6 kJ mol^{-1} and -52.7 kJ mol^{-1}. The magnetic moments have also been estimated. The calculated electronic structures indicate that the magnetic moment reduction at the Fe(4c) site by the Si substitution at Fe(4c) site is indirect through the neighboring carbon atom, whereas at the Fe(8d) site it is direct.

Contents

Abstract…….…… i

Contents……..……ii

Nomenclature……..iv

1 Introduction……...……..….**1**

1.1 Aim of the Work.……..……...…...……..….1

1.2 Thermodynamics and Kinetics...…….……..……..2

1.3 Previous Work.……...…..…..…….13

Ⅱ First Principles Calculation……...……...……..….**15**

2.1 Historical Background.……...……...……...…..….15

2.1.1 Quantum Mechanics.……..…15

2.1.2 The Born-Oppenheimer Approximation.……..……..17

2.1.3 Many-electron Systems...……...18

2.2 The Density Functional Theory.……...……...……...19

2.2.1 The Hohenberg-Kohn Theorem..……20

2.2.2 The Kohn-Sham Equation.……...…...23

2.2.3 The Exchange-Correlation Functional.……26

2.3 The Full-Potential Linearized Augmented Plane-Wave (FLAPW) Method.…….....30

2.3.1 Choosing Basis Functions.…….....31

2.3.2 The Bloch Theorem.……32

2.3.3 The FLAPW Method.……...…….…..…….37

2.4 Computational Model and Method..……...…...40

Ⅲ Results and Discussions…..……43

3.1 Computational Parameters...……...……43

3.2 Lattice Parameter Optimization...……...……...….44

3.3 The Formation Energy..…….……57

3.4 Bulk Moduli.……...……...66

3.5 Magnetic Properties……..……..……...68

Ⅳ Conclusions……..……..……...79

References……..……81

Appendix…….……86

Acknowledgements……..……..88

Curriculum Vitae……...……89

Nomenclature

3D-BZ	Three dimensional Brillouin zone
A_1	Eutectoid temperature
A_2	Curie point
A_3	The temperature at which ferrite transforms to austenite
A_4	The temperature at which austentite transforms to ferrite
Ac	The critical temperature for cooling process
Ae	The critical temperature for equilibrium
Ar	The critical temperature for heating process
B	Bulk modulus
B'	The pressure derivative of bulk modulus
BCC	Body centered cubic
DOS	Density of states
E_{coh}	Cohesive energy
E_{GS}	The ground state energy
$E[n]$	Energy density functional
$E_{xc}[n]$	Exchange-correlation density functional
$E(\mathrm{Fe}_l\mathrm{M}_m\mathrm{C}_n)$	The total energy at equilibrium state
E_F	Fermi energy level
FCC	Face centered cubic
Fe_3C	Cementite
$(\mathrm{Fe}_{11}\mathrm{M}_{\mathrm{Fe}}^{4c})\mathrm{C}_4$	Structure with an iron atom which is replaced by M at 4c
$(\mathrm{Fe}_{11}\mathrm{M}_{\mathrm{Fe}}^{8d})\mathrm{C}_4$	Structure with an iron atom which is replaced by M at 8d
$(\mathrm{Fe}_{11}\mathrm{Si}_{\mathrm{Fe}}^{4c})\mathrm{C}_4$	Structure with an iron atom which is replaced by Si at 4c
$(\mathrm{Fe}_{11}\mathrm{Si}_{\mathrm{Fe}}^{8d})\mathrm{C}_4$	Structure with an iron atom which is replaced by Si at 8d
$(\mathrm{Fe}_{11}\mathrm{Al}_{\mathrm{Fe}}^{4c})\mathrm{C}_4$	Structure with an iron atom which is replaced by Al at 4c
$(\mathrm{Fe}_{11}\mathrm{Al}_{\mathrm{Fe}}^{8d})\mathrm{C}_4$	Structure with an iron atom which is replaced by Al at 8d

$(Fe_{11}Mn_{Fe}^{4c})C_4$	Structure with an iron atom which is replaced by Mn at 4c
$(Fe_{11}Mn_{Fe}^{8d})C_4$	Structure with an iron atom which is replaced by Mn at 8d
FM	Ferromagnetic
GGA	Generalized gradient approximation
H_{tot}	Total sum of Hamiltonian
$\boldsymbol{k}$	Reciprocal lattice vectors
LDA	Local density approximation
LDOS	Projected local density of states
MT	Muffin-tin
$n(\boldsymbol{r})$	Electronic density function
n_{hom}	Electron density value for homogeneous electrons
n_{GS}	The ground state electronic density
NM	Nonmagnetic
$\boldsymbol{R}$	Bravais lattice vectors
T_n	Nuclei kinetic part of Hamiltonian
T_e	Electronic kinetic part of Hamiltonian
ΔU	The formation energy
$u_l(r)$	Radial part to express inside muffin-tin sphere
$V_{n\text{-}n}$	Interaction part between nuclei and nuclei
$V_{e\text{-}e}$	Interaction part between nuclei and electrons
$V_{n\text{-}e}$.	Interaction part between electrons and electrons
V_{ext}	External potential
V_{eff}	Effective potential
$Y_{lm}(\theta, \varphi)$	Spherical harmonics
α	Ferrite
γ	Austenite
Ψ	Wave function of Schrödinger equation
Ψ_n	Wave function of nuclei part of Schrödinger equation

Ψ_e	Wave function of electronic part of Schrödinger equation
Ψ_{GS}	The ground state wave function
Ψ_e	Wave function of electronic part of Schrödinger equation
Ψ_{GS}	The ground state wave function
Ψ_{min}^{n}	The wave function which give the minimum value of kinetic and electronic interaction part with density n

Ⅰ Introduction

1.1 Aim of the Work

Steels are usually combinations of body-centered-cubic (BCC) ferrite, face-centered-cubic (FCC) austenite and orthorhombic cementite (Fe_3C) phases. The concentrations of solutes and thermo-mechanical processing of the steel determine the fractions of each phase and the details of the microstructure. The phases and microstructure can in turn determine properties such as strength, toughness and hardenability. Cementite can be detrimental in many strong steels and mechanisms must be found to suppress its formation during the evolution of the final microstructure.

There is a particular mixture of phases in steels which has led to dramatic developments in their application (Matsumura *et al.*, 1987; Caballero *et al.*, 2001; Speer *et al.*, 2004, Caballero *et al.*, 2004; Jacques, 2004; Yang *et al.*, 2005; De Cooman, 2004; Chatterjee, 2007). This combination is commonly designated carbide-free bainite and consists of a mixture of fine ferrite plates, embedded in a matrix of carbon-retained austenite. This latter phase is usually unstable at room temperature, but is made so by preventing cementite precipitation using silicon and aluminum addition to the steel. The austenite is then able to retain carbon in solid solution, allowing it to stay untransformed to room temperature.

The specific role of silicon in retarding cementite precipitation has been known for a long time (Bain, 1939; Allten and Payson, 1953; Owen, 1954; Matas and Hehemann, 1961; Entin, 1962; Keh and Leslie, 1963; Deliry, 1965; Pomey, 1966; Gordine and Codd, 1969; Hehemann, 1970; Le-Houillier *et al.*, 1971; Lorimer *et al.*, 1972; Sandvik, 1982; Bhadeshia and Edmonds, 1983).

During precipitation of cementite at low temperature, it must maintain the silicon concentration of the parent phase; since the solubility of silicon in cementite is almost zero, the entrapping of silicon is thought to dramatically decrease the driving force for precipitation (Bhadeshia, 2003; Ghosh and Olson, 2002; Kozeschnik and Bhadeshia, 2008).

However, it has not been possible to theoretically support the mechanism by which the silicon acts, because thermodynamic data on silicon in cementite cannot be measured due to its incredibly low solubility in the carbide. Values based on educated guesses are used in the limited calculations that exist (Ghosh and Olson, 2002; Kozeschnik and Bhadeshia, 2008). The purpose of this work was specifically to derive the relevant thermodynamic data using total energy calculations, in particular, by using the all-electron full-potential linearized augmented plane-wave (FLAPW) method (Wimmer *at al.*, 1981; Weinert *at al.*, 1928) implemented in the QMD-FLAPW package.

1.2 Thermodynamics and Kinetics

The study of steels and irons usually begins with the iron-carbon diagram. Fig. 1.1 is the iron-carbon system metastable diagram. In steel systems, many of the properties are determined by the phases and microstructures which appear in this diagram. These factors also influence the behavior not only in iron-carbon system but also more complex alloy systems, both equilibrium and para-equilibrium transformation. The phases which are found in the iron-carbon diagram can be found also in complex steels, but alloying elements will affect the formation and properties of these phases.

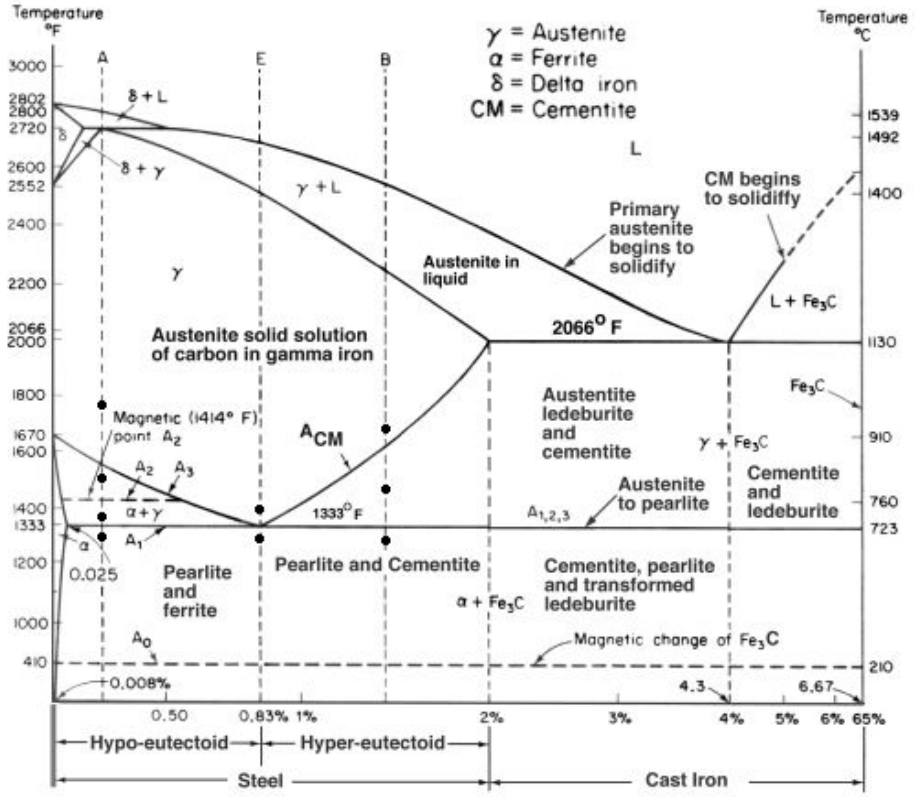

Figure 1.1 An iron-carbon system metastable equilibrium diagram (Pollack, 1988).

There are several important phases in the iron-carbon system such as BCC ferrite at low temperatures (α-ferrite) and high temperature (δ-ferrite), FCC austenite (γ-austenite) and cementite (θ-carbide). There are several critical temperatures in the iron-carbon phase diagram. First, there is the A_1 temperature which represents the eutectoid at about 723℃ in the binary system. Second, A_2 is the Curie point at which ferritic iron transforms from its ferromagnetic state to become paramagnetic at about 769℃. The third point is the A_3 temperature at which ferrite transforms to austenite at about 910℃ in pure iron. The last point is A_4 when austenite transforms to δ-

ferrite, 1390℃ for pure iron. These temperatures can be determined for heating (Ac), cooling (Ar) and equilibrium (Ae). The alloying elements change the shape and critical temperatures on the phase diagram, and indeed, may lead to the introduction of new phases and multiphase equilibria.

The alloying elements can be classified as four groups according to the binary phase diagrams with iron, as two groups of ferrite formers and austenite formers. Fig. 1.2 represents four categories of alloying elements with respect to the phase diagram with iron. Class 1 (Fig. 1.2.a) is for open γ-field which makes γ-phase more stable. The elements nickel, manganese, cobalt and ruthenium, rhodium, palladium, osmium, iridium and platinum of this group eliminate the ferrite phase and replace it with the austenite phase so, depress the phase transformation from γ to α, i.e. both Ae_1 and Ae_3 temperatures are lowered. Class 2 (Fig. 1.2.b) is for expanded γ-field which also makes γ-phase stable. The γ-field is expanded, but there is a limiting temperature for the existence of the γ-phase, and a critical concentration for expansion; likewise carbon, nitrogen, copper, zinc and gold. These classes 1 and 2 are γ-stabilizers. Class 3 (Fig. 1.2.c) is for a closed γ-field and contains silicon, aluminum, beryllium and phosphorus. These elements help the formation of ferrite and restrict the formation of the γ-phase, so the α-ferrite and δ-ferrite phase fields are connected. Class 4 (Fig. 1.2.d), in which boron is the most significant element but includes tantalum, niobium and zirconium, are for a contracted γ-field. Class 3 and class 4 solutes are classified as α-stabilizers.

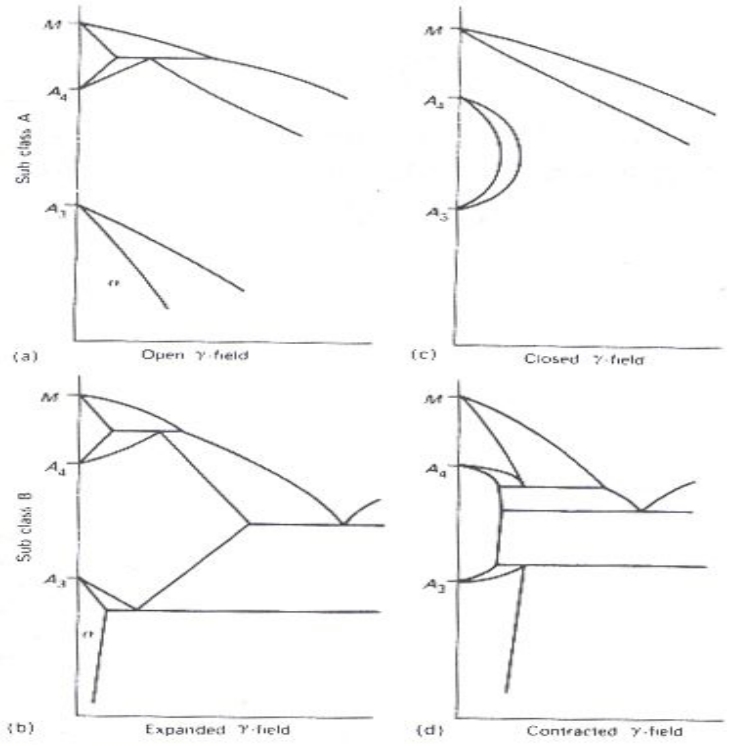

Figure 1.2 Classification of iron alloy phase diagrams: (a) open γ-field (b) expanded γ-field (c) closed γ-field (d) contracted γ-field (Honeycombe and Bhadeshia, 2006)

Zener and Andrews described these behaviors using the formation enthalpy (Bhadeshia and Honeycombe, 2006). Let ΔH is the enthalpy change which is the formation energy per unit of solute dissolving in γ-phase minus the formation energy per unit of solute dissolving in α-phase. A ferrite former has a positive value of ΔH, whereas an austenite former has a negative. Fig. 1.3 is the classification of ferrite and austenite formers.

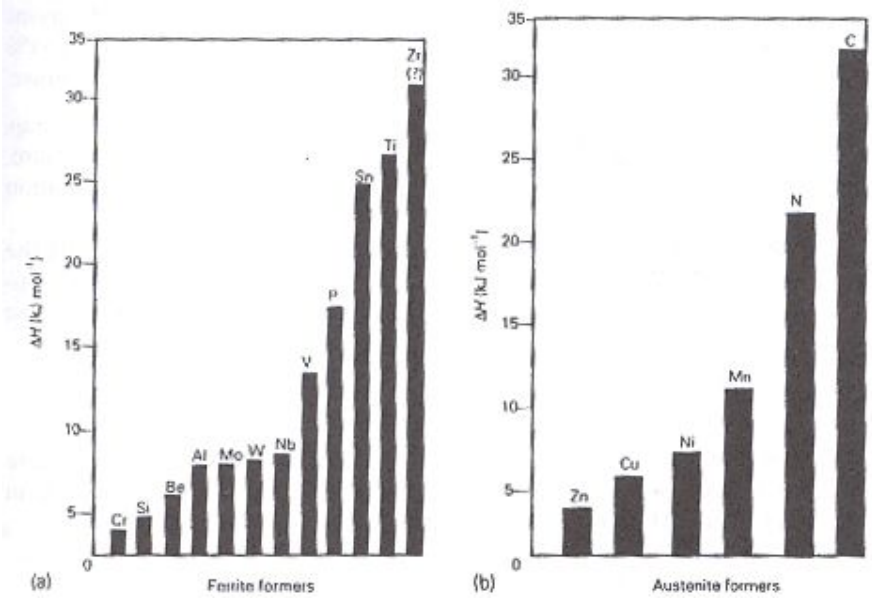

Figure 1.3 Relative strength of alloying elements as (a) ferrite formers (b) austenite formers (Honeycombe and Bhadeshia, 2006).

Silicon and aluminum encourage the formation of BCC iron (ferrite), and they are contained in the categories of class 3 in Fig. 1.2. In the transformation from austenite to ferrite with cementite, silicon and aluminum enter only the ferrite phase. These elements are also used to suppress the formation of cementite. Silicon is usually added to steels in the range 1.5 – 2.5 wt% to retard the formation of cementite and to retain austenite. Aluminum also decreases the rate of cementite precipitation (Leslie, 1977) so there have been attempts to substitute it for silicon.

If manganese is added in sufficiently large quantities, ferrite is replaced by austenite at ambient temperature, Fig. 1.2. In the transformation from austenite to ferrite with cementite, manganese enters into solid solution in cementite instead of forming manganese carbide. The growth process from

austenite to ferrite occurs with partition and local equilibrium at the transformation interface. Manganese increases the solubility of carbon in austenite, but high concentrations of manganese induce carbide precipitation in austenite.

Figs. 1.4 – 1.6 show calculated equilibrium ternary phase diagrams of Fe-C-[Si, Al, Mn] at 773K, respectively, using MTDATA, which is a Gibbs free energy minimization algorithm developed the National Physical Laboratory, U.K. with TCFE database. In the minimization process, only cementite and austenite have been allowed. The tie lines in cementite-austenite equilibrium region are connected with concentration points of pure Fe_3C, but the tie lines of Fe-Mn-C systems are connecting the equilibrium region from Fe_3C to Mn_3C.

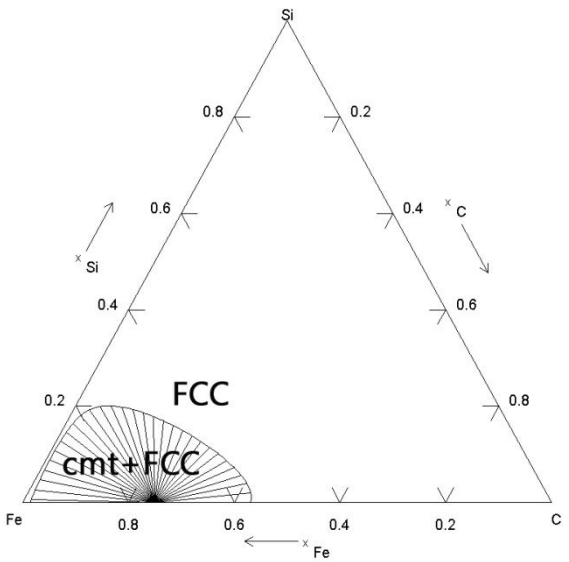

Figure 1.4 Ternary phase diagram of Fe-Si-C system at 773 K. Only austenite and cementite are permitted to exist.

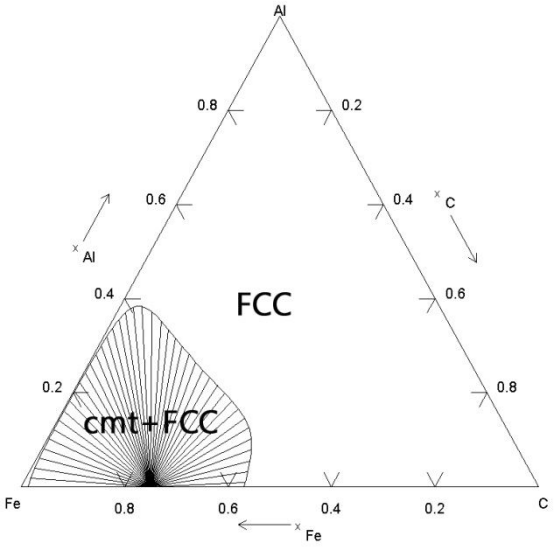

Figure 1.5 Ternary phase diagram of Fe-Al-C system at 773 K. Only austenite and cementite are permitted to exist.

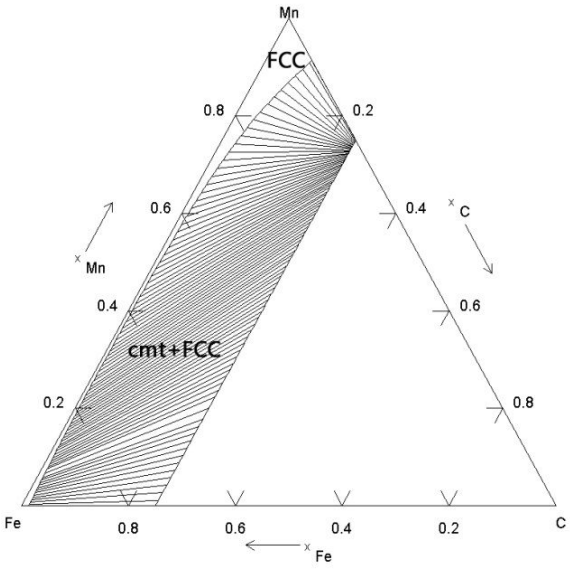

Figure 1.6 Ternary phase diagram of Fe-Mn-C system at 773 K.

Fig. 1.7 is equilibrium and corresponding para-equilibrium phase diagrams when austenite and cementite coexist, using unjustified thermodynamic data for the presence of silicon in cementite (Bhadeshia *et al.*, 2003). It is clear that the single phase austenite field is greatly expanded when transformation is occurred by para-equilibrium mechanism. The solubility of silicon was assumed arbitrarily to be 1 p.p.m. at 298K and other thermodynamic interactions were assumed to be ideal to calculate para-equilibrium transformation. At 773K, the concentration of x-point is in two phase region in equilibrium transformation, but it falls into single phase austenite regions in para-equilibrium. This shows that a silicon addition can dramatically affect the fraction of cementite phase in para-equilibrium conditions.

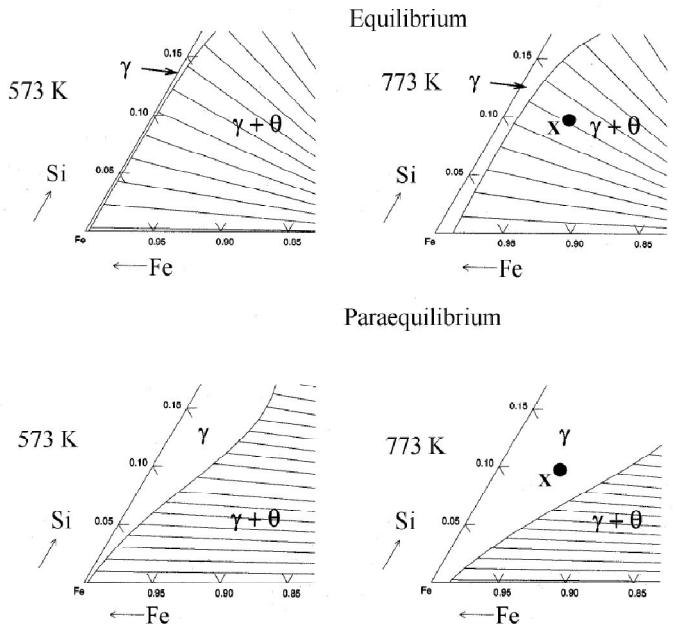

Figure 1.7 Calculated equilibrium and corresponding para-equilibrium phase diagrams for Fe-Si-C system. The concentrations are in mole fractions. (Bhadeshia *et al.*, 2003)

Figs. 1.8 (a) and (b) illustrate the calculation results of silicon and manganese on the fraction of cementite as a function of temperature in equilibrium and para-equilibrium condition, respectively (Kozeschnik and Bhadeshia, 2008). Whereas the equilibrium fractions are a little increased by a silicon addition, there are dramatic changes for the para-equilibrium condition in which silicon atoms are trapped inside the cementite lattice. In contrast, the addition of manganese has a smaller effect on the cementite fraction at para-equilibrium cases compared with a silicon addition.

Fig. 1.9 is a schematic Gibbs free energy graph of austenite and cementite as a function of carbon concentration to illustrate the fraction of cementite results. The fraction of cementite is determined by using the lever rule on the tangential line with cementite chemical potential point and austenite curve. At equilibrium condition, since the solubility of silicon in cementite is very low, the concentration and chemical potential of cementite will be the same as with pure cementite. Therefore, almost all of the silicon will be in the austenite and ferrite phases, and increase the free energies of austenite and ferrite. As a consequence the equilibrium carbon concentration of austenite is lowered and the fraction of cementite is a little increased. However, with the para-equilibrium condition (silicon atoms do not partition between the phases), trapped silicon makes cementite much less stable relative to austenite.

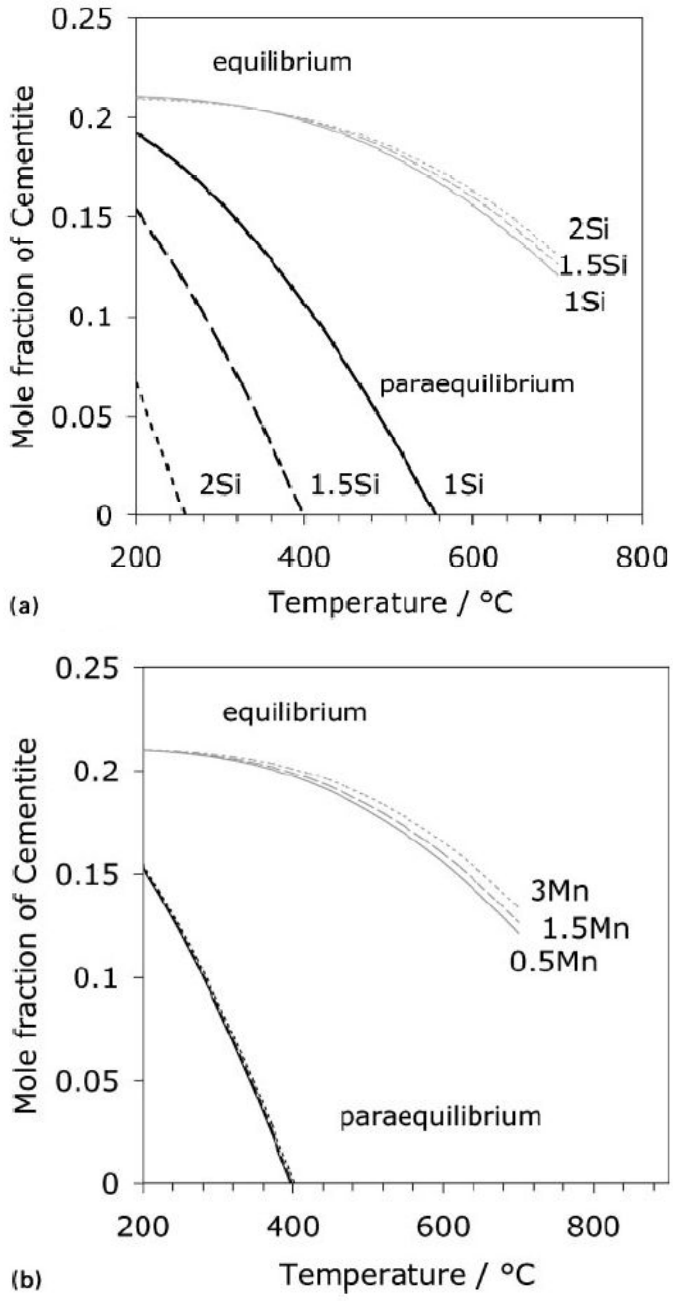

Figure 1.8 Calculated phase fraction of cementite in equilibrium or para-equilibrium with austenite, in system Fe-Si-Mn-C with base composition Fe-1.2C-1.5Mn-1.5Si (wt%) (Kozeschnik and Bhadeshia, 2008).

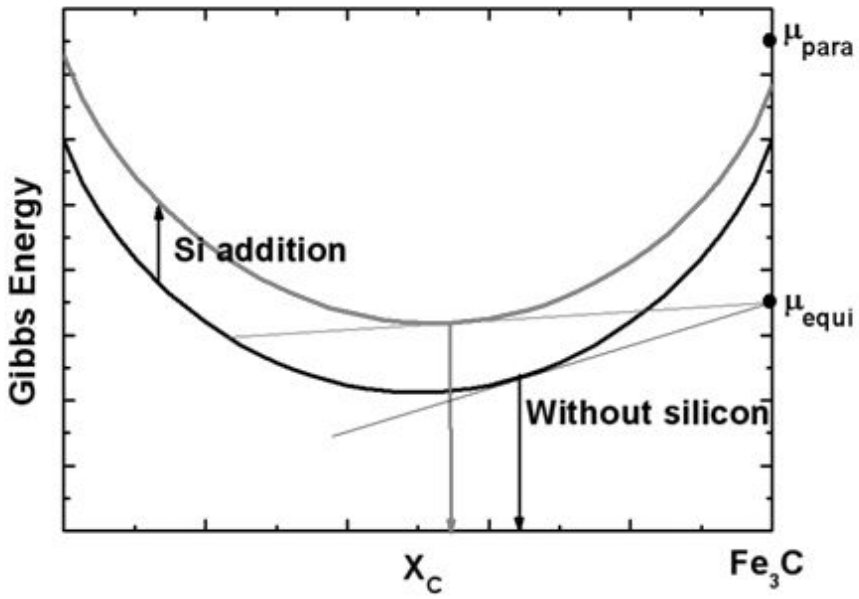

Figure 1.9 A schematic Gibbs free energy graph of austentite and cementite as a function of carbon concentration.

1.3 Previous Work

As seen in Fig. 1.11, the crystal structure of cementite is orthorhombic with space group *Pnma* and its empirical lattice constants are known to be $a = 5.0896$ Å, $b = 6.7443$ Å and $c = 4.5248$ Å (Fasiska and Jeffrey, 1965). Cementite has four Fe atoms taking Fe(4c) positions which are not equivalent to the Fe(8d) locations of the other eight Fe atoms, and four C atoms located at C(4c) positions (Fasiska and Jeffrey, 1965; Herbstein and Smuts, 1964).

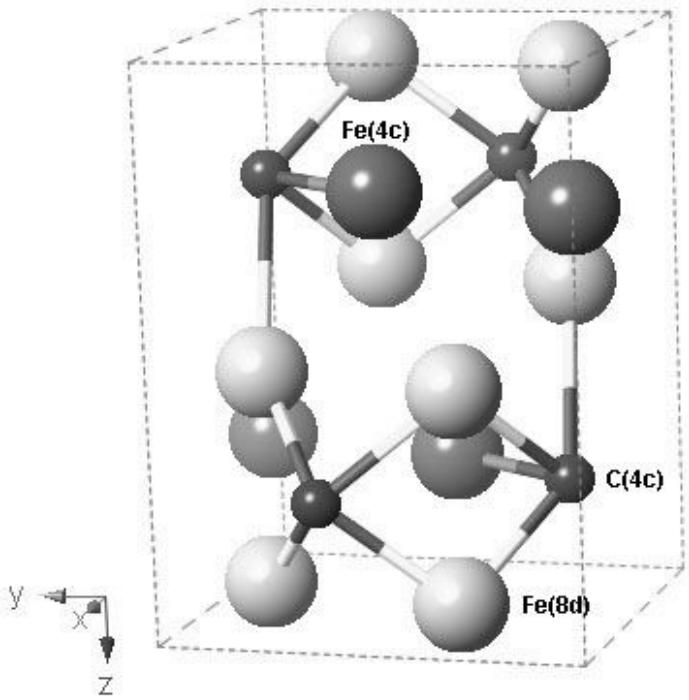

Figure 1.11 Crystal structure of cementite. The dark small spheres, the dark big spheres, and the light big spheres represent C(4c), Fe(4c) and Fe(8d) atoms, respectively. (Jang *et al*, 2008)

The crystal structures, atomic positions, formation energies and magnetic properties of η-carbide (Fe_2C), χ-carbide (Fe_2C_5) and cementite (Fe_3C) have been calculated using first-principles calculations. An ab-initio study on pure cementite using the linear muffin-tin orbital (LMTO) method has indicated the magnetic moments in the ferromagnetic state to be $1.98\ \mu_B$, $1.74\ \mu_B$ and $-0.06\ \mu_B$ for the Fe(4c), Fe(8d) and the carbon atoms, respectively. The calculated cohesive energy per atom, E_{coh}, was found to be 8.37 eV (Haglund *et al.*, 1991). The calculated bulk modulus is found to be 235 GPa and the magnetic moment to be $5.77\ \mu_B$ (Faraoun, 2006). The transition from the metallic ferromagnetic to the paramagnetic state occurs at about 483 K (Tsuzuki, 1984).

The replacement of Cr into cementite has formerly been investigated; the Fe(8d) positions were found to be the favored sites for Cr, whose occupancy enhance the atomic interactions in Fe_3C leading to a considerable change in the local distribution of the electron density according to the self consistent full-potential LMTO (FP-LMTO) method (Medvedeva, 2006).

Ⅱ First Principles Calculation

2.1 Historical Background

Classical theories based on empirical or semi-empirical methods have in the past provided valuable understanding about the properties and phenomena of materials such as the thermodynamics of chemical vapor deposition (Hwang *et al.*, 1992), abnormal grain growth (Hwang *et al.*, 1998), multi-component diffusion (Lee, 1999), interfacial reaction (Lee, 1999) and spinodal decomposition (Hilliard, 1970). However, the importance of a quantum mechanical treatment is increasing as the scale of interest decreases towards the nano-scales. But even more importantly, as we come to realize that certain properties cannot be measured experimentally for materials of any scale, because of the lack of precision in methods or some other phenomenon which are not experimentally accessible. The most fundamental information, for example, structural, mechanical, electrical, vibrational, thermal and optical properties, of a given crystal is related with its electronic structure which can be achieved by solving Schrödinger equation. It should at the same time be emphasized that such calculations are not a panacea and there are many more problems which are best treated using macroscopic theories such as those involving dislocations.

2.1.1 Quantum Mechanics

The study of quantum mechanics seems to have begun from Planck's radiation law, the Einstein-Debye theory of specific heats, the Bohr atom, de Broglie's matter waves together with careful analyses of some key experiments such as the Compton effect, the Franck-Hertz experiment, and the Davisson-Germer-Thompson experiment (Sakurai, 1994). After some

decades, Heisenberg, Schrödinger, Dirac and Feynman succeeded in formulating quantum mechanics mathematically. Dirac described the quantum mechanics using an infinite dimensional Hilbert space which consists of bra and ket vectors, and regarding the observables as self adjoint linear operators which contains the Hamiltonian operator. An element, which represents a physical state and contains all the information of the state, in this infinite dimensional vector space can be expressed as a function known as the Schrödinger wave-function, $\Psi(r)$, which is also a normalized eigenfunction of the Hamiltonian operator.

The fundamental interaction of solids is known well to be the electromagnetic interaction. The solid consists of nuclei and electrons which are somewhat pragmatically classified two groups; valence electrons which contribute to chemical bonding and core electrons which are tightly bound in the closed shells of the lattice nuclei. In principle, the solution of the many-body time-dependent and time-independent Schrödinger equations with electrons and nuclei, for a given solid, gives all possible time-dependent and time-independent information, respectively. However, it is impractical to solve the many-body coupled-equation directly.

The Hamiltonian of a solid consists of the nuclei kinetic T_n, the electronic kinetic T_e part and the interaction part between the nuclei $V_{n\text{-}n}$ and electrons $V_{e\text{-}e}$ with nuclei-electrons interaction $V_{n\text{-}e}$.

$$H_{tot} = T_n + V_{n\text{-}n} + T_e + V_{e\text{-}e} + V_{n\text{-}e} \tag{2.1}$$

$$H_{tot} = -\sum_i \frac{1}{2}\nabla_i^2 + \frac{1}{2}\sum_{i\neq j}\frac{1}{|\boldsymbol{r_i}-\boldsymbol{r_j}|} - \sum_I \frac{1}{2M_I}\nabla_I^2 + \frac{1}{2}\sum_{I\neq J}\frac{Z_I Z_J}{|\boldsymbol{R_I}-\boldsymbol{R_J}|} - \sum_{i,I}\frac{Z_I}{|\boldsymbol{r_i}-\boldsymbol{R_I}|}. \tag{2.2}$$

The Hamiltonian in Eq. (2.2) is subjected to the time-dependent or time-independent Schrödinger equation

$$H_{tot}\Psi(\{\boldsymbol{R_I}\},\{\boldsymbol{r_i}\};t\} = E_{tot}\Psi(\{\boldsymbol{R_I}\},\{\boldsymbol{r_i}\};t\} \tag{2.3}$$

$$H_{tot}\Psi\big(\{\boldsymbol{R_I}\},\{\boldsymbol{r_i}\}\big) = E_{tot}\Psi\big(\{\boldsymbol{R_I}\},\{\boldsymbol{r_i}\}\big)\ , \tag{2.4}$$

where Ψ is the normalized eigenfunction of the Hamiltonian operator H_{tot}. Since the Schrödinger equation (2.3) and (2.4) have complex structure, it is necessary to use a variety of approximations to reach a practical solution.

2.1.2 The Born-Oppenheimer Approximation

The masses of the nuclei of the solid are heavy with respect to those of the electrons, so nuclei by comparison have almost no wave-like properties. The nuclei are not much affected by the movements of the electrons, but the electrons do respond to the motions of the nuclei. Therefore, it is possible to approximate the positions of nuclei as being fixed, with respect to the electron motion. This is the so-called *adiabatic* or *Born-Oppenheimer approximation* (Born, 1926; Born and Oppenheimer, 1930; Jost and Pais, 1951; Kohn, 1954), and lead to the decoupling of Eqs (2.3) and (2.4) into the electronic and nuclei components.

When it is assumed that the eigenfunction Ψ of the Hamiltonian H_{tot} is

$$\Psi(\{\boldsymbol{R_I}\},\{\boldsymbol{r_i}\};t\} = \Psi_n(\{\boldsymbol{R_I}\};t)\,\Psi_e(\{\boldsymbol{r_i}\}\,|\,\{\boldsymbol{R_I}\}) \tag{2.5}$$

$$\Psi\big(\{\boldsymbol{R_I}\},\{\boldsymbol{r_i}\}\big) = \Psi_n(\{\boldsymbol{R_I}\})\,\Psi_e(\{\boldsymbol{r_i}\}\,|\,\{\boldsymbol{R_I}\}), \tag{2.6}$$

where Ψ_n is a function depending only on the position of the lattice nuclei, Eqs (2.3) and (2.4) can be solved approximately using (Michael, 1994)

$$\{T_e + V_{e\text{-}e} + V_{n\text{-}e}(\{\boldsymbol{R_I}\})\}\,\Psi_e = E_e(\{\boldsymbol{R_I}\})\,\Psi_e \tag{2.7}$$

$$\{T_n + V_{n\text{-}n} + E_e(\{\boldsymbol{R_I}\})\}\,\Psi_n = E_{tot}\,\Psi_n. \tag{2.8}$$

Eqs (2.7) and (2.8) represent the adiabatic approximation of the solid. Most problems in solid state physics are reduced to the solution of Eq. (2.7), with *N*-electrons permeating a given static nucleus array, in a solid.

2.1.3 Many-electron Systems

The most general way to solve the many-body solid state problems is the application of the finite temperature quantum field theory (QFT) of relativistic particles (Kapusta, 1989). However, it is difficult to achieve an exact solution and has had limited applications to electron gases, liquids and elementary solids (Anderson, 1997; Zinn-Justin, 1997). One of the earliest and most widely used approximations for Ψ is due to Hartree (1928), who approximated the many-electron wave function as a product of single-particle functions, i.e.,

$$\Psi(\boldsymbol{r_1},,\cdots,\boldsymbol{r_N}) = \Psi_1(\boldsymbol{r_1})\cdots\Psi_N(\boldsymbol{r_N}). \tag{2.9}$$

Each of the functions Ψ_i satisfies a one-electron Schrödinger equation

$$\left[-\tfrac{1}{2}\nabla^2 + V_{ext} + \Phi_i\right]\Psi_i(\boldsymbol{r}) = \varepsilon_i\Psi_i(\boldsymbol{r})\,, \tag{2.10}$$

where the Coulomb potential Φ_i is given by Poisson's equation

$$\nabla^2\Phi_i = 4\pi\textstyle\sum_{j=1,j\neq i}^{N}|\,\Psi_i\,|^2, \tag{2.11}$$

V_{ext} is the potential due to the nuclei. This picture has been modified applying the Pauli exclusion principle (Fock, 1930). An extension of the Hartree-Fock method, known to be the GW approximation, suggested by Quinn and Ferrel (1958) and then Hedin (1965) has been developed based on this approximation.

In the mid 1960's, new approach for obtaining the ground state of a given many electron system was suggested by Hohenberg and Kohn (1964). The density functional theory (DFT) treats the electron density of a system as the basic variable in the electronic problem instead of the wave functions; the problem is then reformulated to a single quasi-electron Schrödinger-like equation (Kohn and Sham, 1965) to obtain the appropriate energy functional of the system. The efficiency of the DFT in calculation makes it popular in the field of electronic structure theory.

2.2 The Density Functional Theory

In principle, the time-independent static properties can be determined from the time-independent Schrödinger Eq. (2.7) when assuming the Born-Oppenheimer approximation to be valid. Eq. (2.7) can be rewritten as

$$\{T_e + V_{e\text{-}e} + \sum_{i=1}^{N} V_{ext}(\boldsymbol{r_i})\}\, \Psi(\boldsymbol{r_1}, \cdots, \boldsymbol{r_N}) = E\Psi(\boldsymbol{r_1}, \cdots, \boldsymbol{r_N}) \qquad (2.12)$$

$$\int \Psi^*(\boldsymbol{r_1}, \boldsymbol{r_2}, \cdots, \boldsymbol{r_N})\Psi(\boldsymbol{r_1}, \boldsymbol{r_2}, \cdots, \boldsymbol{r_N})\mathrm{d}\boldsymbol{r_1} \cdots \mathrm{d}\boldsymbol{r_N} = 1, \qquad (2.13)$$

where, $\boldsymbol{r_i}$ is the position of the ith electron, N is the total number of electrons, V_{ext} is the external field in which the electrons move which is the electrostatic potential generated by the nuclei, whose positions are assumed fixed and whose spatial movements are assumed negligible. E is the total

electronic energy. Although considering only spatial coordinates in order to simplify the problem, Eq. (2.12), it is still impossible to solve in the general case. The eigenfunction Ψ depends on 3N position coordinates, but most experimental observables depend only on the one-electron density function (Michel, 1995)

$$n^{(1)}(\boldsymbol{r},\boldsymbol{r}') = N\int \Psi^*(\boldsymbol{r},\boldsymbol{r_2},\cdots,\boldsymbol{r_N})\Psi(\boldsymbol{r}',\boldsymbol{r_2},\cdots,\boldsymbol{r_N})\mathrm{d}\boldsymbol{r_2}\cdots\mathrm{d}\boldsymbol{r_N} \qquad (2.14)$$

or the two-electron density function

$$n^{(2)}(\boldsymbol{r_1},\boldsymbol{r_2},\boldsymbol{r_1'},\boldsymbol{r_2'}) = \frac{N(N-1)}{2}\int \Psi^*(\boldsymbol{r_1},\boldsymbol{r_2},\cdots,\boldsymbol{r_N})\Psi(\boldsymbol{r_1'},\boldsymbol{r_2'},\cdots,\boldsymbol{r_N})\mathrm{d}\boldsymbol{r_3}\cdots\mathrm{d}\boldsymbol{r_N} \qquad (2.15)$$

and most noteworthy is the electron density in position space

$$n(\boldsymbol{r}) = n^{(1)}(\boldsymbol{r},\boldsymbol{r}) \qquad (2.16)$$

$$\int n(\boldsymbol{r})\mathrm{d}\boldsymbol{r} = N \qquad (2.17)$$

Therefore, Ψ with 3N parameters gives much more detailed information than is actually needed in practical applications, and it would simplify calculations if the redundant information can be avoided by finding the solution with 3 parameters.

2.2.1 The Hohenberg-Kohn Theorem

Hohenberg and Kohn (1964) derived the basic theorems of the density functional formalism that the electron density $n(\boldsymbol{r})$ determines uniquely the external potential $V_{ext}(\boldsymbol{r})$ using a variational principle. This implies that the electron density in three-dimensional position space is sufficient in

constructing the Hamiltonian operator of Eq. (2.12) since electron kinetic part T_e and electron-electron interaction contribution $V_{e\text{-}e}$ is determined by electron density naturally, but $V_{ext}(\boldsymbol{r})$ is not. Thus, $n(\boldsymbol{r})$ determines any ground-state properties and any ground-state property is a functional of $n(\boldsymbol{r})$. Let Ψ^n_{min} gives the minimum value of $<\Psi|T+V_{ee}|\Psi>$ for all Ψ such that $n(\boldsymbol{r}) = N\int \Psi^*\Psi \mathrm{d}\boldsymbol{r_2}\cdots\mathrm{d}\boldsymbol{r_N}$, and be a functional $E[n]$ as

$$E[n] \equiv \int V_{ext}(\boldsymbol{r})n(\boldsymbol{r})\mathrm{d}\boldsymbol{r} + <\Psi^n_{min}|T+V_{ee}|\Psi^n_{min}>. \tag{2.18}$$

Let be E_{GS}, Ψ_{GS} and n_{GS} to be the ground-state energy, wave function, and density, respectively. Then, the Hohenberg and Kohn theorems can be formulated as

$$<\Psi\left|\textstyle\sum_{i=1}^{N} V_{ext}(\boldsymbol{r_i})\right|\Psi> = \int V_{ext}(\boldsymbol{r})n(\boldsymbol{r})\mathrm{d}\boldsymbol{r},$$

$$\forall\Psi, \text{ which satisfies } n(\boldsymbol{r}) = N\int \Psi^*\Psi \mathrm{d}\boldsymbol{r_2}\cdots\mathrm{d}\boldsymbol{r_N} \tag{2.19}$$

$$E[n] \geq E_{GS},\ \forall n(\boldsymbol{r}) \tag{2.20}$$

$$E[n_{GS}] = E_{GS} \tag{2.21}$$

Eqs (2.19-2.21) can be proven as following (Jones and Gunnarsson, 1989).

Since $T_e + V_{e\text{-}e} + \sum_{i=1}^{N} V_{ext}(\boldsymbol{r_i})$ is symmetric which has no difference of changing coordinate vectors in Eq. (2.12), $\Psi(\boldsymbol{r_1},\cdots,\boldsymbol{r_N})$ also must be a symmetric function. Therefore it can be redefined $n(\boldsymbol{r})$ as

$$n(\boldsymbol{r_i}) = N\int \Psi^*\Psi \mathrm{d}\boldsymbol{r_1}\cdots\boldsymbol{r_{i-1}}\boldsymbol{r_{i+1}}\cdots\mathrm{d}\boldsymbol{r_N}\ , \tag{2.22}$$

for arbitrary chosen i. Then

$$
\begin{aligned}
< \Psi \left| \sum_{i=1}^{N} V_{ext}(\boldsymbol{r_i}) \right| \Psi > &= \sum_{i=1}^{N} < \Psi | V_{ext}(\boldsymbol{r_i}) | \Psi > \\
&= \sum_{i=1}^{N} \int \Psi^* V_{ext}(\boldsymbol{r_i}) \Psi \mathrm{d}\boldsymbol{r_1} \cdots \mathrm{d}\boldsymbol{r_N} \\
&= \sum_{i=1}^{N} \frac{1}{N} \int V_{ext}(\boldsymbol{r_i})\, n(\boldsymbol{r_i}) \mathrm{d}\boldsymbol{r_i} \\
&= \int V_{ext}(\boldsymbol{r}) n(\boldsymbol{r}) \mathrm{d}\boldsymbol{r}. \qquad (2.23)
\end{aligned}
$$

Writing $V = \sum_{i=1}^{N} V_{ext}(\boldsymbol{r_i})$,

$$
\begin{aligned}
E[n] &= \int V_{ext}(\boldsymbol{r}) n(\boldsymbol{r}) \mathrm{d}\boldsymbol{r} + < \Psi_{min}^{n} | T + V_{ee} | \Psi_{min}^{n} > \\
&= < \Psi_{min}^{n} \left| \sum_{i=1}^{N} V_{ext}(\boldsymbol{r_i}) \right| \Psi_{min}^{n} > + < \Psi_{min}^{n} | T + V_{ee} | \Psi_{min}^{n} > \\
&= < \Psi_{min}^{n} | V + T + V_{ee} | \Psi_{min}^{n} > \qquad (2.24)
\end{aligned}
$$

A Ψ_{min}^{n} may not be an eigenfunction of the Hamiltonian operator $V + T + V_{ee}$, but it can be expanded as a linear combination of the actual eigenfunctions $\{\Psi_n\}$, which is orthonormalized, of the operator which is a self-adjoint linear operator.

$$
\Psi_{min}^{n} = \sum_n C_n \Psi_n. \qquad (2.25)
$$

To find the expectation value of $V + T + V_{ee}$, Eq. (2.24) can be changed to

$$
\begin{aligned}
< \Psi_{min}^{n} | V + T + V_{ee} | \Psi_{min}^{n} > &= < \sum_n C_n \Psi_n | H | \sum_m C_m \Psi_m > \\
&= \sum_{n,m} < C_n \Psi_n | E_m | C_m \Psi_m > \\
&= \sum_{n,m} C_n^* C_m E_m < \Psi_n | \Psi_m > \\
&= \sum_n |C_n|^2 E_n \\
&\geq E_{GS} \sum_n |C_n|^2 \\
&= E_{GS}. \qquad (2.26)
\end{aligned}
$$

This proves the inequality Eq. (2.20). Eq. (2.26) is called the variational

principle. Using the minimum property of the ground state (GS),

$$
\begin{aligned}
E[n_{GS}] &= \int V_{ext}(\boldsymbol{r}) n_{GS}(\boldsymbol{r}) \mathrm{d}\boldsymbol{r} + < \Psi_{min}^{n_{GS}} | T + V_{ee} | \Psi_{min}^{n_{GS}} > \\
&= < \Psi_{min}^{n_{GS}} | V + T + V_{ee} | \Psi_{min}^{n_{GS}} > \\
&\geq E_{GS} \\
&= < \Psi_{GS} | V + T + V_{ee} | \Psi_{GS} > \\
&= \int V_{ext}(\boldsymbol{r}) n_{GS}(\boldsymbol{r}) \mathrm{d}\boldsymbol{r} + < \Psi_{GS} | T + V_{ee} | \Psi_{GS} > \qquad (2.27)
\end{aligned}
$$

and by the definition of $\Psi_{min}^{n_{GS}}$,

$$
< \Psi_{min}^{n_{GS}} | T + V_{ee} | \Psi_{min}^{n_{GS}} > \leq < \Psi_{GS} | T + V_{ee} | \Psi_{GS} >. \qquad (2.28)
$$

Eqs (2.27) and (2.28) show that inequality should be equality, so Eq. (2.21) holds which means $E[n]$ can be a density functional for ground state energy.

This completes the proof of the theorem. Eq. (2.27) shows also that $\Psi_{min}^{n_{GS}}$ should be equal to Ψ_{GS} if the ground state is not degenerate. This proof and theorem is valid only on the ground state since Eq. (2.27) cannot be go further for other states. This theorem provides a general method for calculating the ground-state properties, but they gave information only about existence, but not about the relevant functional. A practical calculation was introduced by Kohn and Sham (1965).

2.2.2 The Kohn-Sham Equation

The total kinetic energy of the system is a ground-state property, and it is a density functional by Hohenberg and Kohn theorem,

$$T = T[n]. \tag{2.29}$$

It is also possible to write the classical electrostatic Coulomb energy for the electron density as a functional of $n(\boldsymbol{r})$,

$$E_C[n] = \frac{1}{2}\iint \frac{n(\boldsymbol{r_1})n(\boldsymbol{r_2})}{|\boldsymbol{r_1}-\boldsymbol{r_2}|}\mathrm{d}\boldsymbol{r_1}\mathrm{d}\boldsymbol{r_2} = \frac{1}{2}\int n(\boldsymbol{r_1})V_C(\boldsymbol{r_1})\,\mathrm{d}\boldsymbol{r_1} \tag{2.30}$$

$$V_C(\boldsymbol{r_1}) = \int \frac{n(\boldsymbol{r_2})}{|\boldsymbol{r_1}-\boldsymbol{r_2}|}\mathrm{d}\boldsymbol{r_2}, \tag{2.31}$$

therefore Eq. (2.18) can be rewritten as follows,

$$\begin{aligned} E[n] &= \int V_{ext}(\boldsymbol{r})n(\boldsymbol{r})\mathrm{d}\boldsymbol{r} + < \Psi^n|T + V_{ee}|\Psi^n > \\ &= \int V_{ext}(\boldsymbol{r})n(\boldsymbol{r})\mathrm{d}\boldsymbol{r} + T[n] + E_C[n] + E_{xc}[n] \\ &= \int V_{ext}(\boldsymbol{r})n(\boldsymbol{r})\mathrm{d}\boldsymbol{r} + T[n] + \frac{1}{2}\int V_C(\boldsymbol{r})n(\boldsymbol{r})\mathrm{d}\boldsymbol{r} + E_{xc}[n]. \end{aligned} \tag{2.32}$$

where $E_{xc}[n]$ is exchange-correlation functional which is everything not contained in the other term, and its approximation determines the quality of practical applications and their results.

To have a minimum value of $E[n]$ with constraint of Eq. (2.17), Eq. (2.32) should follow the Lagrange multiplier principle. From the definition of functional derivative, it can be obtained

$$\frac{\delta}{\delta n}\int V_{ext}(\boldsymbol{r})n(\boldsymbol{r})\mathrm{d}\boldsymbol{r} = \frac{\partial}{\partial n}\big(V_{ext}(\boldsymbol{r})n(\boldsymbol{r})\big) = V_{ext}(\boldsymbol{r}) \tag{2.33}$$

$$\frac{\delta E_C[n]}{\delta n} = \frac{\partial}{\partial n}\left(\int \frac{n(\boldsymbol{r_1})n(\boldsymbol{r_2})}{2|\boldsymbol{r_1}-\boldsymbol{r_2}|}\mathrm{d}\boldsymbol{r_2}\right) = \int \frac{n(\boldsymbol{r_2})}{|\boldsymbol{r_1}-\boldsymbol{r_2}|}\mathrm{d}\boldsymbol{r_2} = V_C(\boldsymbol{r}) \tag{2.34}$$

$$\frac{\delta}{\delta n}\int n(\boldsymbol{r})\mathrm{d}\boldsymbol{r} = \frac{\partial}{\partial n}\big(n(\boldsymbol{r})\big) = 1. \tag{2.35}$$

By variational principle, $E[n]$ should have minimum value at ground state

electron density,

$$\frac{\delta E[n]}{\delta n} = V_{ext}(\boldsymbol{r}) + \frac{\delta T[n]}{\delta n} + V_C(\boldsymbol{r}) + \frac{\delta E_{xc}[n]}{\delta n} = \mu \frac{\delta}{\delta n} \int n(\boldsymbol{r}) \mathrm{d}\boldsymbol{r} = \mu \quad (2.36)$$

where μ is Lagrange multiplier. Kohn and Sham compared this result with that obtained for N non-interacting fictitious particles, moving in another external effective potential V_{eff} , which gives the same energy of the considering electronic system, but without inter-particle interactions. The equivalent of equation (2.36) is in this case,

$$\frac{\delta E[n]}{\delta n} = \frac{\delta \tilde{T}[n]}{\delta n} + V_{eff}(\boldsymbol{r}) = \mu, \quad (2.37)$$

where $\tilde{T}[n]$ is the kinetic energy of these non-interacting particles. The advantage of the fictitious particles is that it is possible to solve the Schrödinger equation which is a single-particle equation of the form

$$\left[-\frac{1}{2}\nabla^2 + V_{eff}\right] \Psi_i(\boldsymbol{r}) = \varepsilon_i \Psi_i(\boldsymbol{r}). \quad (2.38)$$

The ground state for this system by occupying the N energetically lowest single particle and the total density is given by

$$n(\boldsymbol{r}) = \sum_{i=1}^{N} \Psi_i^*(\boldsymbol{r}) \Psi_i(\boldsymbol{r}). \quad (2.39)$$

Comparing the Eq. (2.36) with Eq. (2.37), the effective potential given by

$$\begin{aligned} V_{eff}(\boldsymbol{r}) &= V_{ext}(\boldsymbol{r}) + V_C(\boldsymbol{r}) + \frac{\delta E_{xc}[n]}{\delta n} + \left(\frac{\delta T[n]}{\delta n} - \frac{\delta \tilde{T}[n]}{\delta n}\right) \\ &\equiv V_{ext}(\boldsymbol{r}) + V_C(\boldsymbol{r}) + \frac{\delta E_{xc}{}'[n]}{\delta n} \end{aligned}$$

$$\equiv V_{ext}(\boldsymbol{r}) + V_C(\boldsymbol{r}) + V_{xc}(\boldsymbol{r}). \tag{2.40}$$

where $V_{xc}(\boldsymbol{r})$ is the exchange-correlation potential

$$V_{xc}(\boldsymbol{r}) = \frac{\delta E_{xc}'[n]}{\delta n} \tag{2.41}$$

as well as

$$E_{xc}'[n] = E_{xc}[n] + T[n] - \tilde{T}[n]. \tag{2.42}$$

2.2.3 The Exchange-Correlation Functional

Now, the remaining major problem in solving Eq. (2.7) is to find $V_{xc}(\boldsymbol{r})$. The exact functionals for exchange and correlation are not known except for the free electron gas. V_{xc} and E_{xc}' are functionals of the electron density $n(\boldsymbol{r})$, and may depend on the behaviour of $n(\boldsymbol{r})$ in the whole space not only the local distribution. In physics, the mostly widely used approximation is the local density approximation (LDA), suggested by Hedin and Lundqvist (1971) based on the assumption that $V_{xc}(\boldsymbol{r})$ depends on the local electron density at the point $\boldsymbol{r}$. V_{xc} at the point $\boldsymbol{r}$ is calculated as for the homogeneous electron gas with the density of that point,

$$n_{hom} = n(\boldsymbol{r}) \tag{2.43}$$

It is possible to obtain the complete form of $V_{xc}[n_{hom}]$ and $E_{xc}'[n_{hom}]$, which are functions of n_{hom}, dependence on the number n_{hom} considering a homogeneous electron gas (Michel, 1995). Therefore, the following approximated form is suggested,

$$E_{xc}'[n(\boldsymbol{r})] = \int \varepsilon_{xc}(n(\boldsymbol{r}))n(\boldsymbol{r})\mathrm{d}\boldsymbol{r} \tag{2.44}$$

where $\varepsilon_{xc}(n_{hom}) = \varepsilon_{xc}\big(n(\boldsymbol{r})\big)$ is the exchange-correlation energy per electron of a homogeneous electron gas with uniform density of Eq. (2.43).

Even though the LDA has in fact been found to give good results for a broad range of systems, its derivation shows that it is appropriate only for free and nearly free electron systems such as simple metals which closely resemble the homogeneous electron gas. Therefore, for strongly correlated systems (e.g. materials containing atoms with 3*d* or 4*f* electrons such as transition metals including Fe-systems and rare-earth systems), it is necessary to develop another method. There have been many attempts to improve upon the LDA functional.

Among the most successful achievement have been the Generalized Gradient Approximations (GGA), the so-called PW91 scheme of Perdew and Wang (1991) and the PBE scheme of Perdew, Burke and Ernzerhof (1996). The definition of functional derivative gives following formula,

$$\frac{\delta}{\delta n}\left(\int f(\boldsymbol{r}, n(\boldsymbol{r}), \nabla n(\boldsymbol{r}), \cdots, \nabla^N n(\boldsymbol{r}))\right) = \frac{\partial f}{\partial n} - \nabla \cdot \frac{\partial f}{\partial(\nabla n)} + \nabla^2 \cdot \frac{\partial f}{\partial(\nabla^2 n)} - \cdots, \tag{2.45}$$

therefore LDA can be treated as the first term approximation of Eq. (2.45) for V_{xc}. The improvement of this approximation can be achieved by treating the second term approximation, i.e.

$$E_{xc}'[n(\boldsymbol{r})] = \int f(n(\boldsymbol{r}), \nabla n(\boldsymbol{r}))\mathrm{d}\boldsymbol{r}. \tag{2.46}$$

Eq. (2.46) is the general form of exchange-correlation functional of GGA

scheme. Unlike the LDA scheme, where the energy functional has a known form, the form $\int f(n(\boldsymbol{r}), \nabla n(\boldsymbol{r}))$ is unfixed. There is a large amount of variations in determining their form, since there is no specific physical system to fit. A variety of exchange-correlation functional, referred to as mPWPW91, B3LYP, MPW1K, PBE1PBE, BLYP, and PBE, have developed for calculations on specific classes of system, but since the choice is dependent on the problem the calculations are not truly first. Table 2.1 shows the list of the exchange-correlation functionals.

	Name	Equation
LDA	WVWN	$1.0E_x$(Slater) + $1.0E_c$(VWN)
GGA	BLYP	$1.0E_x$(Slater) + $1.0\Delta E_c$(B88) + $1.0E_C$(LYP)
	BP86	$1.0E_x$(Slater) + $1.0\Delta E_c$(B88) + $1.0E_C$(PZ81,local) + $1.0\Delta E_c$(B86,nonlocal)
	BPW91	$1.0E_x$(Slater) + $1.0\Delta E_c$(B88) + $1.0E_C$(PW91)
	PWPW	$1.0E_x$(Slater) + $1.0\Delta E_c$(PW91) + $1.0E_C$(PW91)
	mPWPW	$1.0E_x$(Slater) + $1.0\Delta E_c$(mPW) + $1.0E_C$(PW91)
	PBEPBE	$1.0E_x$(Slater) + $1.0\Delta E_c$(PBE) + $1.0E_C$(PW91,local) + $1.0\Delta E_c$(PBE,nonlocal)
	XLYP	$1.0E_x$(Slater) + $1.0\Delta E_c$(B88) + $0.347E_C$(PW91) + $1.0E_c$(LYP)
Hybrid	BH&HLYP	$0.5E_x$(HF) + $0.5E_x$(Slater) + $0.5\Delta E_x$(B88) + $1.0E_c$(LYP)
	B3LYP	$0.2E_x$(HF) + $0.8E_x$(Slater) + $0.72\Delta E_x$(B88) + $0.19E_C$(VWN) + $0.81E_C$(LYP)
	B3P86	$0.2E_x$(HF) + $0.8E_x$(Slater) + $0.72\Delta E_x$(B88) + $1.0E_C$(VWN) + $0.81E_C$(LYP)
	B3PW91	$0.2E_x$(HF) + $0.8E_x$(Slater) + $0.72\Delta E_x$(B88) + $1.0E_C$(PW91,local) + $0.81\Delta E_C$(PW91,nonlocal)
	PW1PW1	$0.25E_x$(HF) + $0.75E_x$(Slater) + $0.72\Delta E_x$(PW91) + $1.0E_C$(PW91)
	mPW1PW	$0.25E_x$(HF) + $0.75E_x$(Slater) + $0.72\Delta E_x$(mPW91) + $1.0E_C$(PW91)
	PBE1PBE	$0.25E_x$(HF) + $0.75E_x$(Slater) + $0.72\Delta E_x$(PBE) + $1.0E_C$(PW91,local) + $1.0\Delta E_C$(PBE,nonlocal)
	X3LYP	$0.218E_x$(HF) + $0.782E_x$(Slater) + $0.542\Delta E_x$(B88) + $0.167\Delta E_x$(PW91) + $0.219E_C$(VWN) + $0.871E_C$(LYP)

Table 2.1: Summary of the exchange-correlation functional (Lee, 2006).

2.3 The Full-Potential Linearized Augmented Plane-Wave (FLAPW) Method

Now, the problem of solving many electron problems has been changed to an eigenvalue problem of single particle Kohn-Sham equation, Eqs (2.38) and (2.40).

$$\left[-\frac{1}{2}\nabla^2 + V_{ext}(\boldsymbol{r}) + V_C(\boldsymbol{r}) + V_{xc}(\boldsymbol{r})\right]\Psi_i(\boldsymbol{r}) = \varepsilon_i\Psi_i(\boldsymbol{r}). \qquad (2.47)$$

A lot of methods have been proposed for solving Eq. (2.47) for different applications, geometries, symmetries, chemical elements and materials requiring different approximations (Blügel, 2006). Fig. 2.1 shows roughly an overview of electronic structure methods.

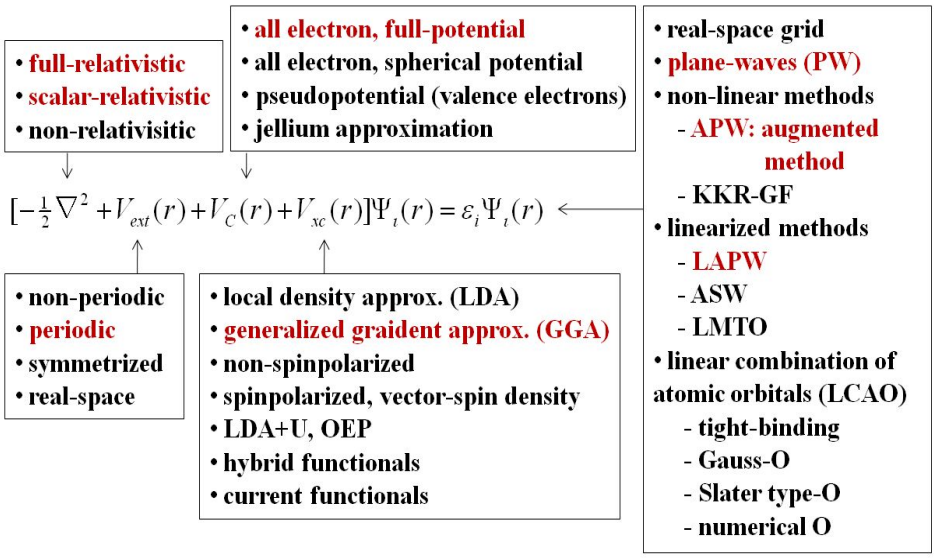

Figure 2.1 Overview of electronic structure calculations (Blügel, 2006).

2.3.1 Choosing Basis Functions

The last task of the eigenvalue problem Eq. (2.47) is choosing basis function sets $\{\varphi_n(\boldsymbol{r})\}$ for $\Psi_i(\boldsymbol{r})$,

$$\Psi_i(\boldsymbol{r}) = \sum C_n \, \varphi_n(\boldsymbol{r}). \tag{2.48}$$

Using Eq. (2.48), the partial differential equation (2.47) can be solved through algebraic equations which gives the values of C_i's. A lot of candidates for $\{\varphi_i(\boldsymbol{r})\}$ have been suggested. The plane-waves can be one of choice, since they are the eigenstates of a translation operator in the solid through the Bloch theorem (Slater, 1972; Ashcroft and Mermin, 1976). The other method such as linear combination of atomic orbital (LCAO) method (Bloch, 1928), the Wigner-Seitz method (1933) which is sometimes called the cellular method, the orthorgonalized plane-wave (OPW) method (Herring, 1940), the method of pseudopotential (PP) theory (Phillips and Kleinman, 1959), the mixed basis (MB) method (Brwon, 1962), the augmented plane-wave (APW) method (Slater, 1937; Saffren and Slater, 1953), KKR method which means Korringa (1947) and Kohn and Rostoker (1954) and full-potential LAPW (FLAPW) method (Wimmer, Krakauer and Freeman, 1981) have been used for electronic structure calculation.

The convergence of the summation in Eq. (2.48) depends on the similarity of choice and real solution. For example, in treating isolated clusters or molecules, methods based on localized orbitals or Gaussian function sets are frequently selected with the chemical intuition of the system, and a plane-waves set, which is used in pseudopotential and LAPW method, converges efficiently to the density of valence electrons in the system which is three dimensional periodic symmetries such as solid state (Bloch, 1928). Although

the plane-waves set is a good choice for illustrating valence electrons, it diverges as $\frac{1}{r}$ at the nucleus and have a singular point at the center of nucleus, where r represents the distance from nucleus (Blügel, 2006).

The pseudopotential method substitutes a singular potential near nucleus to a smooth potential by changing a nucleus to an ion which consists of nucleus and core electrons. Therefore, it is popular in the field of simple metals or semi-conductor material systems which contain carbon or silicon. However, for ferromagnetic materials and complex metals such as Fe, not only valence electrons but also core electrons which are tightly bound to the nucleus influence the properties of the entire system. This means that it is necessary to introduce another basis function to represent the bound electrons. The LAPW method divides the whole space to inside muffin-tin (MT) sphere, which is illustrated using spherical harmonics that are the same with atomic orbital shapes, and outside which is well approximated using plane-waves (Koelling and Arbman, 1975; Andersen, 1975). Therefore the LAPW method is the one of the most accurate method for all electrons and can treat transition metal including Fe systems with complex electron structure, although it demands more computational cost than others.

2.3.2 The Bloch Theorem

For the system which follows the Born-von Karman periodic boundary conditions, for all (x_1, x_2, x_3) and not only eigenfunction, but also any function $\Psi(\boldsymbol{r})$,

$$\begin{aligned}\Psi(x_1 + L_1, x_2, x_3) &= \Psi(x_1, x_2, x_3)\\ \Psi(x_1, x_2 + L_2, x_3) &= \Psi(x_1, x_2, x_3)\\ \Psi(x_1, x_2, x_3 + L_3) &= \Psi(x_1, x_2, x_3),\end{aligned} \tag{2.49}$$

the eigenfunction $\Psi_{\boldsymbol{k}}$ of the one-electron Hamiltonian $H = -\frac{1}{2}\nabla^2 + U(\boldsymbol{r})$, where $U(\boldsymbol{r}) = U(\boldsymbol{R} + r)$ for all $\boldsymbol{R}$ in a Bravais lattice, can be chosen to have the form of a plane-wave times a function with the periodicity of the Bravais lattice (Ashcroft and Mermin, 1976), i.e.

$$\Psi_{\boldsymbol{k}}(\boldsymbol{r}) = e^{i\boldsymbol{k}\cdot\boldsymbol{r}} u_{\boldsymbol{k}}(\boldsymbol{r}), \tag{2.50}$$

where $u_{\boldsymbol{k}}(\boldsymbol{r}) = u_{\boldsymbol{k}}(\boldsymbol{R} + \boldsymbol{r})$ for all $\boldsymbol{R}$ in the Bravais lattice, and Eq. (2.50) also implies that

$$\Psi_{\boldsymbol{k}}(\boldsymbol{r} + \boldsymbol{R}) = e^{i\boldsymbol{k}\cdot(\boldsymbol{r}+\boldsymbol{R})} u_{\boldsymbol{k}}(\boldsymbol{r} + \boldsymbol{R}) = e^{i\boldsymbol{k}\cdot\boldsymbol{r}} e^{i\boldsymbol{k}\cdot\boldsymbol{R}} u_{\boldsymbol{k}}(\boldsymbol{r}) = e^{i\boldsymbol{k}\cdot\boldsymbol{R}} \Psi_{\boldsymbol{k}}(\boldsymbol{r}). \tag{2.51}$$

The Bloch theorem is equivalent to an alternative form that there exists an eigenstate $\boldsymbol{k}$ for each $\Psi_{\boldsymbol{k}}$ such that,

$$\Psi_{\boldsymbol{k}}(\boldsymbol{r} + \boldsymbol{R}) = e^{i\boldsymbol{k}\cdot\boldsymbol{R}}\, \Psi_{\boldsymbol{k}}(\boldsymbol{r}). \tag{2.52}$$

for every $\boldsymbol{R}$ in the Bravais lattice.

The Bloch theorem can be proved as follows. Let $\mathbf{a_1} + \mathbf{a_2} + \mathbf{a_3}$ be the primitive Bravais lattice and $\boldsymbol{R_n} = n_1\mathbf{a_1} + n_2\mathbf{a_2} + n_3\mathbf{a_3}$, $\boldsymbol{R_m} = m_1\mathbf{a_1} + m_2\mathbf{a_2} + m_3\mathbf{a_3}$ for any integers n_i and m_j. Then there exist the minimum integer N_i which satisfies

$$N_i a_i = L_i \tag{2.53}$$

where $a_i = |\boldsymbol{a_i}|$ and L_i from Eq. (2.49). Let $T_{\boldsymbol{R_n}}$ be a translation operator which operating on any function $\Psi(\boldsymbol{r})$ shifts by $\boldsymbol{R_n}$, i.e.

$$T_{\boldsymbol{R_n}}\Psi(\boldsymbol{r}) = \Psi(\boldsymbol{R_n} + \boldsymbol{r}). \tag{2.54}$$

Since the Hamiltonian has a periodicity of $(\mathbf{a_1}, \mathbf{a_2}, \mathbf{a_3})$,

$$\begin{aligned} T_{\boldsymbol{R_n}}H(\boldsymbol{r})\Psi(\boldsymbol{r}) &= H(\boldsymbol{R_n} + \boldsymbol{r})\Psi(\boldsymbol{R_n} + \boldsymbol{r}) \\ &= H(\boldsymbol{r})\Psi(\boldsymbol{R_n} + \boldsymbol{r}) = H(\boldsymbol{r})T_{\boldsymbol{R_n}}\Psi(\boldsymbol{r}). \end{aligned} \tag{2.55}$$

Because Eq. (2.55) holds for any function Ψ,

$$T_{\boldsymbol{R_n}}H(\boldsymbol{r}) = H(\boldsymbol{r})T_{\boldsymbol{R_n}}. \tag{2.56}$$

In addition, the result of applying two successive translations does not depend on the order in which they are applied, since for any $\Psi(\boldsymbol{r})$

$$T_{\boldsymbol{R_n}}T_{\boldsymbol{R_m}}\Psi(\boldsymbol{r}) = T_{\boldsymbol{R_m}}T_{\boldsymbol{R_n}}\Psi(\boldsymbol{r}) = \Psi(\boldsymbol{R_n} + \boldsymbol{R_m} + \boldsymbol{r}) = T_{\boldsymbol{R_n}+\boldsymbol{R_m}}\Psi(\boldsymbol{r}). \tag{2.57}$$

Eqs (2.56) and (2.57) show that the set of translation operators $T_{\boldsymbol{R_n}}$ and the Hamiltonian H form set of commuting linear operators. Since this follows the fundamental theorem of quantum mechanics that simultaneous diagonalization of commuting operators in an infinite dimensional vector space (Ashcroft and Mermin, 1976), the eigenfunction $\Psi_{\boldsymbol{k}}$, where $\boldsymbol{k}$ is eigenstate index vector, of H can be chosen to be simultaneous eigenfunctions of all the $T_{\boldsymbol{R_n}}$,

$$\begin{aligned} H\Psi_{\boldsymbol{k}} &= \epsilon_k\Psi_{\boldsymbol{k}}, \\ T_{\boldsymbol{R_n}}\Psi_{\boldsymbol{k}} &= c(\boldsymbol{R_n})\Psi_{\boldsymbol{k}} \\ T_{\boldsymbol{R_m}}\Psi_{\boldsymbol{k}} &= c(\boldsymbol{R_m})\Psi_{\boldsymbol{k}} \end{aligned} \tag{2.58}$$

where $c(\boldsymbol{R_n})$ and $c(\boldsymbol{R_m})$ is scalar value since $T_{\boldsymbol{R_n}}\Psi_{\boldsymbol{k}}$ and $T_{\boldsymbol{R_m}}\Psi_{\boldsymbol{k}}$ should represent the same eigenstate with $\Psi_{\boldsymbol{k}}$ and $\Psi_{\boldsymbol{k}}$ is also eigenfunction of translation operator $T_{\boldsymbol{R_n}}$ and $T_{\boldsymbol{R_m}}$. Moreover, according to Eq. (2.57)

$$T_{\boldsymbol{R_n}}T_{\boldsymbol{R_m}}\Psi_{\boldsymbol{k}} = T_{\boldsymbol{R_n}+\boldsymbol{R_m}}\Psi(\boldsymbol{r}) = c(\boldsymbol{R_n}+\boldsymbol{R_m})\Psi_{\boldsymbol{k}} \tag{2.59}$$

$$T_{\boldsymbol{R_n}}T_{\boldsymbol{R_m}}\Psi_{\boldsymbol{k}} = c(\boldsymbol{R_m})T_{\boldsymbol{R_n}}\Psi_{\boldsymbol{k}} = c(\boldsymbol{R_n})c(\boldsymbol{R_m})\Psi_{\boldsymbol{k}} \tag{2.60}$$

If follows that the eigenvalues must satisfy

$$c(\boldsymbol{R_n}+\boldsymbol{R_m}) = c(\boldsymbol{R_n})c(\boldsymbol{R_m}) = c(\boldsymbol{R_m})c(\boldsymbol{R_n}), \tag{2.61}$$

and the set of $c(\boldsymbol{R_n})$ makes an Abelian group with regarding $c(\boldsymbol{0}) = \boldsymbol{I}$ as the identity and $c(-\boldsymbol{R_n})$ as an inverse element with respect to multiplicative operation. If we consider one coordinate and Eq. (2.53),

$$c(n_i\boldsymbol{a_i}) = (c(\boldsymbol{a_i}))^{\boldsymbol{n_i}} \tag{2.62}$$

$$c(N_i\boldsymbol{a_i}) = \boldsymbol{I}. \tag{2.63}$$

Eqs (2.62) and (2.63) means that the set of $c(n_i\boldsymbol{a_i})$ builds a finite cyclic subgroup of $c(\boldsymbol{R_n})$ with respect to multiplication and $c(\boldsymbol{a_i})$ is a generator of that subgroup with N_i order (Hungerford, 1973). Therefore $c(\boldsymbol{a_i})$ can be expressed as

$$c(\boldsymbol{a_i}) = e^{\frac{2\pi i}{N_i}} = e^{ix_i} \tag{2.64}$$

where x_i is related to a_i by $x_i = \frac{2\pi}{N_i} = \frac{2\pi a_i}{L_i}$ with ith component of $\boldsymbol{R_n}$

$$c(n_i \boldsymbol{a_i}) = e^{i n_i x_i} \tag{2.65}$$

$$c(\boldsymbol{R_n}) = c(n_1 \boldsymbol{a_1}) c(n_2 \boldsymbol{a_2}) c(n_3 \boldsymbol{a_3}) = e^{i(n_1 x_1 + n_2 x_2 + n_3 x_3)} = e^{i \boldsymbol{k} \cdot \boldsymbol{R_n}} \tag{2.66}$$

where $\boldsymbol{k} = x_1 \boldsymbol{b_1} + x_2 \boldsymbol{b_2} + x_3 \boldsymbol{b_3}$, and the $\boldsymbol{b_i}$ are the reciprocal lattice vectors satisfying $\boldsymbol{b_i} \cdot \boldsymbol{a_j} = \boldsymbol{\delta_{ij}}$, i.e.

$$\begin{aligned} \boldsymbol{b_1} &= \frac{\boldsymbol{a_2} \times \boldsymbol{a_3}}{\boldsymbol{a_1} \cdot (\boldsymbol{a_2} \times \boldsymbol{a_3})}, \\ \boldsymbol{b_2} &= \frac{\boldsymbol{a_3} \times \boldsymbol{a_1}}{\boldsymbol{a_2} \cdot (\boldsymbol{a_3} \times \boldsymbol{a_1})}, \\ \boldsymbol{b_3} &= \frac{\boldsymbol{a_1} \times \boldsymbol{a_2}}{\boldsymbol{a_3} \cdot (\boldsymbol{a_1} \times \boldsymbol{a_2})}. \end{aligned} \tag{2.67}$$

Summarizing Eqs (2.54), (2.58) and (2.66), it has been shown that the eigenfunction $\Psi_{\boldsymbol{k}}$ of H can be chosen so that for every Bravais lattice vector $\boldsymbol{R}$,

$$T_{\boldsymbol{R}} \Psi_{\boldsymbol{k}}(\boldsymbol{r}) = \Psi_{\boldsymbol{k}}(\boldsymbol{R_n} + \boldsymbol{r}) = c(\boldsymbol{R_n}) \Psi_{\boldsymbol{k}}(\boldsymbol{r}) = e^{i \boldsymbol{k} \cdot \boldsymbol{R_n}} \Psi_{\boldsymbol{k}}(\boldsymbol{r}). \tag{2.68}$$

This is precisely Bloch theorem, in the form Eq. (2.52). Let any vector $\boldsymbol{K_m}$ satisfy $\boldsymbol{K_m} = 2\pi(m_1 \boldsymbol{b_1} + m_2 \boldsymbol{b_2} + m_3 \boldsymbol{b_3})$, where m_i are the integer. The scalar product $\boldsymbol{K_m} \cdot \boldsymbol{R_n}$ has the value $2\pi(m_1 n_1 + m_2 n_2 + m_3 n_3) = 2\pi N$ and the addition of $\boldsymbol{K_m}$ to $\boldsymbol{k}$ yields

$$e^{i(\boldsymbol{k} + \boldsymbol{K_m}) \cdot \boldsymbol{R_n}} = e^{i \boldsymbol{k} \cdot \boldsymbol{R_n}}. \tag{2.69}$$

This shows the periodicity of $\boldsymbol{k}$ space. The space of the form $2\pi(x_1 \boldsymbol{b_1} + x_2 \boldsymbol{b_2} + x_3 \boldsymbol{b_3})$, where $0 \leq x_i \leq 1$, named the *first Brillouin zone* can give information of the whole space, and the set of $\frac{\boldsymbol{K_m}}{\boldsymbol{2\pi}}$ is called the *reciprocal-lattice vector*.

2.3.3 The FLAPW Method

There are many possible method to solve Kohn-Sham equations according to the choice of the basis set $\varphi_{\boldsymbol{G}}(\boldsymbol{k},\boldsymbol{r})$ for all reciprocal lattice vectors up $\boldsymbol{G}$ to the largest value of $\boldsymbol{K_{max}}$,

$$\Psi_{\boldsymbol{k},\nu}(\boldsymbol{r}) = \sum_{|\boldsymbol{k}+\boldsymbol{G}|\leq \boldsymbol{K_{max}}} c_{\boldsymbol{k},\nu}^{\boldsymbol{G}} \varphi_{\boldsymbol{G}}(\boldsymbol{k},\boldsymbol{r}). \tag{2.70}$$

where $c_{\boldsymbol{k},\nu}^{\boldsymbol{G}}$ are variational coefficients (Blügel, 2006). Eq. (2.70) is equivalent with Eq. (2.48), and the vector $\boldsymbol{k}$ has the a role of quantum number n. The Bloch theorem gives the most straightforward suggestion for three dimensional periodic solids, which would be to expand the wave function into plane-waves or Fourier series, respectively,

$$\varphi_{\boldsymbol{G}}(\boldsymbol{k},\boldsymbol{r}) = e^{i(\boldsymbol{k}+\boldsymbol{G})\cdot\boldsymbol{r}}. \tag{2.71}$$

The plane-wave basis set has some important advantages that plane-waves are orthogonal so that, the Fast Fourier Transformation (FFT) method can be applied to simplify calculations. However, plane-wave basis sets do not converge with the $1/r$ singularity at the nuclei. Thus, they can only be used in the context of a pseudopotential approximation to the true potential (Phillips and Kleinman, 1959), where the $1/r$ potential has been replaced by an appropriate smooth potential with ions instead of the nuclei.

Slater (1937) developed the Augmented Plane-wave (APW) method in which the space is partitioned into spheres centered at each atom site, which is strongly varying but nearly spherical, the so-called muffin-tins, and into the remaining interstitial region as in Fig. 2.2.

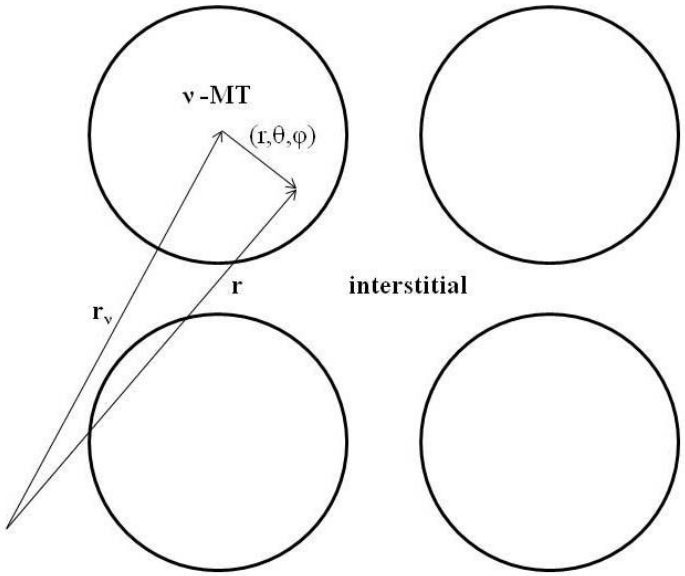

Figure 2.2 The space division both in the APW and LAPW methods.

In the APW method, space is divided into regions and different basis expansions are used in these regions with radial solutions of the Schrödinger equation inside the MT spheres, and plane-waves for the interstices,

$$\varphi_{\boldsymbol{G}}(\boldsymbol{k},\boldsymbol{r}) = e^{i(\boldsymbol{k}+\boldsymbol{G})\cdot\boldsymbol{r}},\ \boldsymbol{r} \in \text{Interstitial}$$
$$\varphi_{\boldsymbol{G}}(\boldsymbol{k},\boldsymbol{r}) = \sum_{\boldsymbol{lm}} A_{lm}^{\nu} u_l(r) Y_{lm}(\theta,\varphi),\ \boldsymbol{r} \in \text{MT sphere } \nu. \quad (2.72)$$

The radial function $u_l(r)$ satisfies

$$\left\{-\frac{\mathrm{d}^2}{\mathrm{d}r^2} + \frac{l(l+1)}{r^2} + V_\nu(r) - E_l\right\} r u_l(r) = 0, \quad (2.73)$$

where V_ν is the spherically symmetric potential inside the ν-th sphere and E_l is the angular momentum dependent energy parameter. The spherical harmonics $Y_{lm}(\theta,\varphi)$, which is used to illustrate an atomic orbital of

hydrogen atom, is the solution of the angular part of Laplace's equation $\nabla^2 f = 0$ (Arfken, 1985). Fig. 2.3 shows the three dimensional shape of $Y_{lm}(\theta, \varphi)$ for $0 \leq m \leq l \leq 3$, which has similar appearance with *s,p,d* and *f* orbitals.

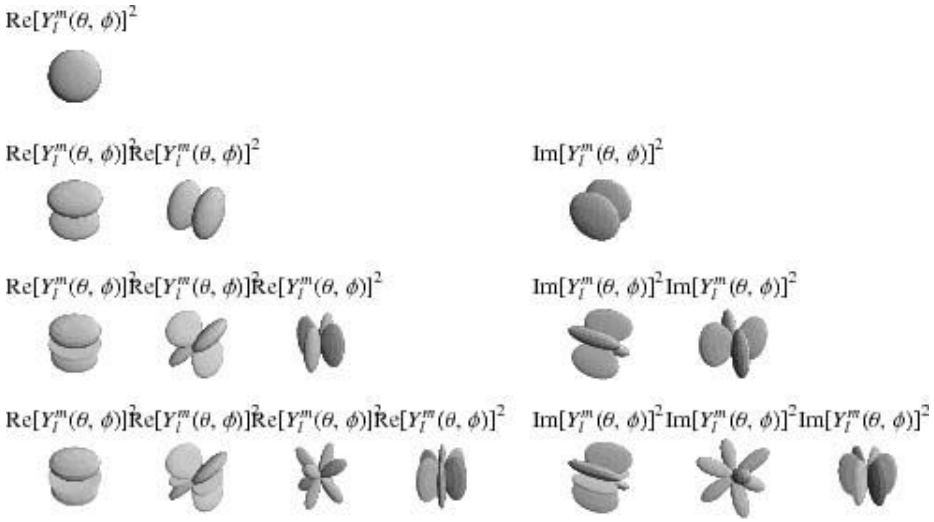

Figure 2.3 Illustrations of $\mathrm{Re}|Y_{lm}(\theta, \varphi)|^2$ and $\mathrm{Im}|Y_{lm}(\theta, \varphi)|^2$ for $0 \leq m \leq l \leq 3$. (http://mathworld.wolfram.com)

The different choice of the basis functions in the different regions demands a boundary condition to be satisfied at the sphere boundary. Hence, A_{lm}^{ν} are completely determined by the energy parameters E_l. Unfortunately, the APWs are solutions inside the spheres only at the energy E_l. This means the lack of variational freedom to allow for changes in the wave function as the band energy deviates for given E_l.

It is required to give the degree of freedom to resolve it, and Koelling and Arbman (1975) and independently Andersen (1975) proposed a linearization method in the radial functions inside the MT sphere, i.e., the basis functions

inside the spheres are linear combinations of $u_l(r)Y_{lm}(\theta,\varphi)$ and its radial derivative $\dot{u}_l(r)Y_{lm}(\theta,\varphi)$.

$$\varphi_{\boldsymbol{G}}(\boldsymbol{k},\boldsymbol{r}) = e^{i(\boldsymbol{k}+\boldsymbol{G})\cdot\boldsymbol{r}},\ \boldsymbol{r} \in \text{Interstitial}$$
$$\varphi_{\boldsymbol{G}}(\boldsymbol{k},\boldsymbol{r}) = \sum_{\boldsymbol{lm}}[A_{lm}^{\nu}u_l(r) + B_{lm}^{\nu}\dot{u}_l(r)]Y_{lm}(\theta,\varphi),\ \boldsymbol{r} \in \text{MT sphere } \nu. \quad (2.74)$$

These functions are matched to the values and derivatives of the plane-waves on the sphere boundaries and the basis functions augmented in the way are the Linearized APW (LAPW) method. The LAPW basis has greater flexibility than the APW method inside the MT sphere, so it avoids the spherical potential approximation. However, higher plane-wave cutoffs are necessary to apply the LAPW method for the non-spherical potential. Harmann (1979) and Weinert (1981) have introduced the full-potential LAPW (FLAPW) method which solves the non spherical potential problem by partitioning the region to vacuum, interstitial and MT sphere regions.

2.4 Computational Model and Method

The Kohn-Sham equations Eq. (2.47) are Schrödinger-like independent-particle equations which give consistent $n(\boldsymbol{r})$ for ground state. The ground state electron density $n_{GS}(\boldsymbol{r})$ that minimizes the energy functional is a fixed point of the mapping

$$n'(\boldsymbol{r}) = F[n(\boldsymbol{r})]. \quad (2.75)$$

where F gives the new electron density from a given $n(\boldsymbol{r})$ and the effective potential determined by $n(\boldsymbol{r})$. This fixed point problem can be solved by iteration. Fig. 2.4 is a schematic flow-chart for self-consistent density functional calculation. A starting density $n^0(\boldsymbol{r})$ can be constructed by atomic

densities. Self consistency can be achieved if the difference of output density $F[n^m(\boldsymbol{r})]$ and input density $n^m(\boldsymbol{r})$ within a sufficiently small error. Convergence can be achieved if the new input density $n^{m+1}(\boldsymbol{r})$ is old input density $n^m(\boldsymbol{r})$ mixed with output density $F[n^m(\boldsymbol{r})]$. The simplest and slowest of such mixing schemes is the simple mixing according to

$$n^{m+1} = (1-\alpha)n^m + \alpha F[n^m], \tag{2.76}$$

where α is the so-called mixing parameter.

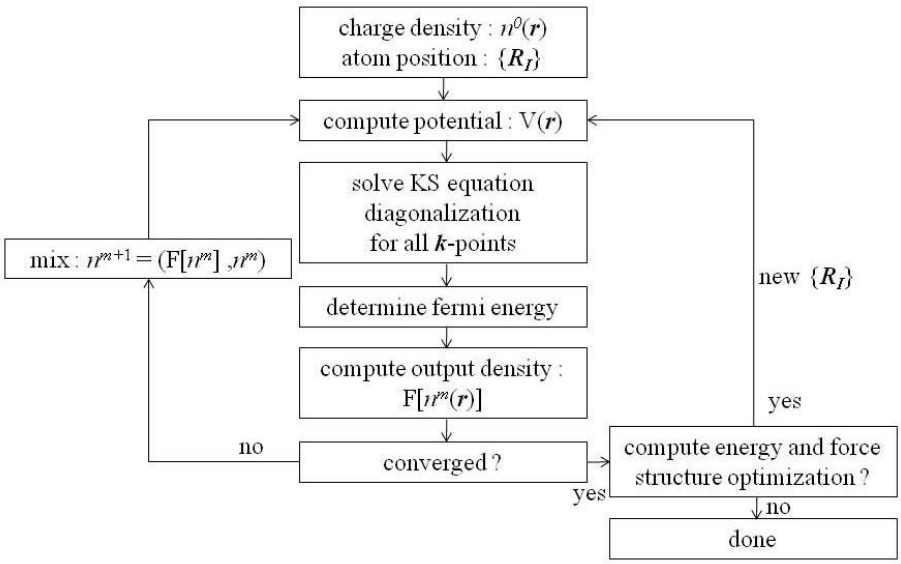

Figure 2.4 Schematic flow-chart for self-consistent density functional calculation (Blügel, 2006)

The CPU time requirement for this process depends on the number of basis functions N, the number of $\boldsymbol{k}$-vectors in the BZ used $N_{\boldsymbol{k}}$ and the number of states M (Blügel, 2006) which are determined by the required precision P

of a calculation and by the volume Ω of the unit cell or the number of atoms in the unit cell, N_A, respectively. Typically the calculation CPU time varies as

$$\text{CPU} \propto N_{iter} N_{\boldsymbol{k}} N^3 \text{ for direct diagonalization}$$
$$\text{CPU} \propto N_{iter} N_{\boldsymbol{k}} M_{iter} (MN \ln N + NM^2) \text{ for iterative diagonalization} \quad (2.77)$$

where M_{iter} gives the number of eigenvalue iterations. The scaling dependencies for precision and to the number of atoms N_A as follows

$$N_{\boldsymbol{k}} \propto {P_{\boldsymbol{k}}}^3 \quad (2.78)$$
$$N \propto P^3 \quad (2.79)$$
$$N_{\boldsymbol{k}} \propto 1/N_A \quad (2.80)$$
$$M \propto N_A \quad (2.81)$$
$$N \propto N_A \quad (2.82)$$

where $P_{\boldsymbol{k}}$ is the precision controlling the $\boldsymbol{k}$-point summation. From these considerations it is the aim to develop an efficient basis to reduce their number N.

Ⅲ Results and Discussions

3.1 Computational Parameters

The unit cell of cementite has an experimental volume of 155.32 $Å^3$ and contains four formula units of Fe_3C, where four iron atoms take 4c positions which are not equivalent to the 8d positions of the other eight iron atoms, and four carbon atoms locate at 4c positions. The 4c positions for iron are linear, while the 8d positions are tri-planar as shown in Fig. 1.11.

The Si, Al and Mn substituted Fe_3C system is simulated by an orthorhombic unit cell with the compositions $(Fe_{11}Si)C_4$, $(Fe_{11}Al)C_4$ and $(Fe_{11}Mn)C_4$ corresponding to a silicon, aluminum and manganese content of 4.07 wt%, 3.92 wt% and 7.67 wt%, respectively. This concentration is only a little higher than the typical concentration in silicon in common transformation induced plasticity steels based on bainite, and the aluminum and manganese concentrations are also reasonable. It is assumed that an alloying element atoms substitute into an iron site, because the atomic radius of Si (1.11 Å), Al (1.18 Å) and Mn (1.61 Å) are similar to that of Fe (1.56 Å), and much larger than that of C (0.67 Å). The location of the alloying atom M in the 4c or 8d site is identified using superscripts: $(Fe_{11}M^{4c}_{Fe})C_4$ and $(Fe_{11}M^{8d}_{Fe})C_4$, where M is Si, Al or Mn. The total energy calculations for the identical Wyckoff positions show essentially the same value within numerical error.

The Kohn-Sham equation was solved self-consistently in terms of the total energy all-electron full-potential linearized augmented plane-wave (FLAPW) method by using the generalized gradient approximation (GGA) for the exchange-correlation potential. The integrations over the three dimensional Brillouin zone (3D-BZ) were performed by the tetrahedron method over a

$9 \times 9 \times 9$ Monkhorst-Pack mesh in the 3D-BZ which corresponds to 125, 205 and 365 k-points inside the irreducible wedge of 3D-BZ for Fe_3C, $(Fe_{11}M_{Fe}^{4c})C_4$ and $(Fe_{11}M_{Fe}^{8d})C_4$, respectively. The degree of precision was obtained by considering a plane-wave cutoff up to 21 Ry, which corresponds to about 1700 linearized augmented plane-waves per each $\boldsymbol{k}$-point and spin. The wave functions, the charge densities, and the potential were expanded with $l \leq 8$ lattice harmonics inside each muffin-tin (MT) sphere with the radii of 2.04 a.u. for Fe, Si, Al, Mn and 1.30 a.u. for C atoms, respectively. The density and potential in the interstitial region were depicted by using a star-function cutoff at 340 Ry. Core electrons were treated fully relativistically, while valence states were calculated scalar relativistically, without considering spin-orbit coupling. Fe semicore states were treated by employing the explicit orthogonalization (XO) scheme for ensuring the orthogonality between the core and valence electrons. Self-consistency was assumed when the root-mean-square distances between the input and output total charges and spin densities were less than 1.0×10^{-5} electrons/a.u.^{3}

The Fe_3C, $(Fe_{11}M_{Fe}^{4c})C_4$ and $(Fe_{11}M_{Fe}^{8d})C_4$ structures were calculated as ferromagnetic for any substitutional element M. The reference states of each system used ferromagnetic body-centered cubic (BCC) iron, nonmagnetic graphite carbon, nonmagnetic diamond silicon, nonmagnetic face-centered cubic (FCC) aluminum and nonmagnetic FCC manganese.

3.2 Lattice Parameter Optimization

The equilibrium lattice constants and the corresponding internal atomic positions were obtained in four steps, beginning with the reported lattice constants and internal coordinates (Fasiska and Jeffrey, 1965). The unit cell volume V was varied using a third order fitting polynomial with the data of

total energy value versus unit cell volume to find out the first step equilibrium volume $V_0^{(1)}$. Then, b/a was modified with the fixed volume $V_0^{(1)}$ to find out the equilibrium b/a. With the constraint obtained, the equilibrium c/a value is obtained. Based on the previously calculated equilibrium lattice variable set $\{V_0^{(1)},\ b/a,\ c/a\}$, the volume optimization was performed with atomic position relaxations by the third order polynomial fitting. This procedure greatly reduces optimization computational time, since it was not performed on the full $\{V,\ b/a,\ c/a\}$ total energy calculation matrix with reasonable precision. The internal atomic positions are relaxed by using the total energy and force minimization scheme using the Broyden method to find the multi-dimensional zero. It was considered a relaxed structure, when the force on each atom was smaller than $2\mathrm{mRy/a.u.}$, and the position did not change more than 3×10^{-3} a.u. The data were fitted to the third order polynomial for simplifying since it can give a good approximation of the shape of Murnaghan's equation (Murnaghan, 1944) with a smaller number of fitting parameters.

Fig. 3.1 shows the calculated total energy versus unit cell volume with the data fitted to the third order polynomial, for both the nonmagnetic (NM) and ferromagnetic (FM) states of cementite. Table 3.1 shows the results of lattice parameter optimization of Fe_3C and calculated internal coordinates compared with experimental values. The calculated unit cell volume of the ferromagnetic Fe_3C is about 2% smaller than the experimental value. Based on the temperature dependent experimental lattice constants (Wood *et al.*, 2004), the extrapolation to zero temperature gives a lattice volume of 154.4Å^3, which is only about 1.4% larger than that calculated.

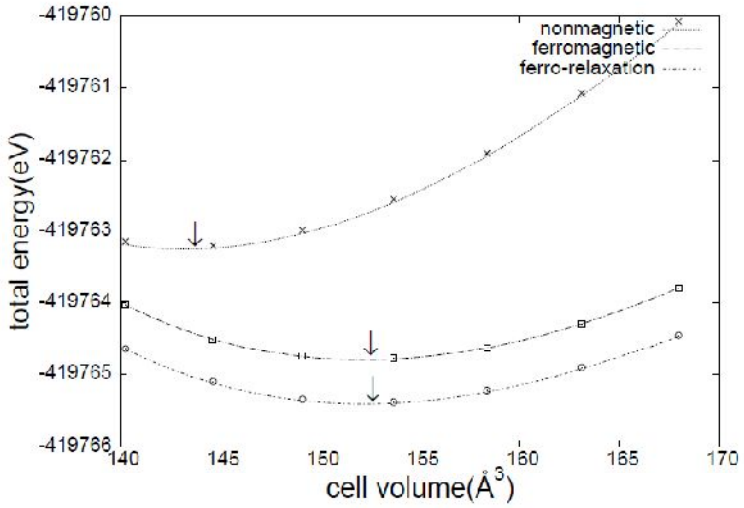

Figure 3.1 Total energy versus unit cell volume of Fe_3C with the optimized values of b/a and c/a. The crosses represent the nonmagnetic results, while the squares represent the ferromagnetic ones with experimental internal coordinates. The circles represent the ferromagnetic ones with optimized internal coordinates. The corresponding lines are third order polynomial fits. The arrows indicate the corresponding equilibrium lattice volumes.

	Fe_3C (measured)	Fe_3C (calculated)
a (Å)	5.0896	5.1281
b (Å)	6.7443	6.6512
c (Å)	4.5248	4.4623
volume ($Å^3$)	155.32	152.20
x_1	0.1816	0.1752
x_2	0.0367	0.0358
x_3	0.1230	0.1236
y_1	0.0666	0.0662
z_1	0.1626	0.1670
z_2	0.1598	0.1602
z_3	0.0560	0.0621

Table 3.1: Calculated equilibrium lattice parameters (in units of Å), unit cell volume (in units of $Å^3$) and internal coordinates (in fractional units) of the Fe_3C cementite crystal structure. The experimental values of the cementite crystal structure are included for reference (Fasiska and Jeffrey, 1965).

Table 3.2 contains the calculation results of equilibrium internal coordinates of Fe_3C with the distance of each atom from one of Fe(4c) and Fe(8d) positions. The calculated shortest interatomic distances of Fe(8d), Fe(4c) and C(4c) from Fe(4c) are 2.495Å, 2.695Å and 2.015Å in Fe_3C, respectively. The distances from Fe(8d) are 2.452Å, 2.495Å and 2.011Å in Fe_3C, respectively. Tables 3.3 – 3.8 show the calculated equilibrium internal coordinates of $(Fe_{11}Si_{Fe}^{4c})C_4$, $(Fe_{11}Si_{Fe}^{8d})C_4$, $(Fe_{11}Al_{Fe}^{4c})C_4$, $(Fe_{11}Al_{Fe}^{8d})C_4$, $(Fe_{11}Mn_{Fe}^{4c})C_4$ and $(Fe_{11}Mn_{Fe}^{8d})C_4$, respectively, with the distances of each atom from substituted atom.

The calculated shortest interatomic distances from substituted Si atom are changed to 2.466Å, 2.669Å and 2.061Å in $(Fe_{11}Si_{Fe}^{4c})C_4$, respectively. In other words, the interatomic distances of Fe(8d) and Fe(4c) measured from Si are contracted 1.2% and 1.0%, respectively, while the distance from C(4c) is expanded 2.3%. Those are calculated to be 2.421Å, 2.466Å and 2.175Å in $(Fe_{11}Si_{Fe}^{8d})C_4$, respectively, which means the distance of Fe(8d) and Fe(4c) from Si are contracted 1.3% and 1.2%, respectively, while the interatomic distance to C(4c) is expanded 8.2 %. These features reveal a general tendency that the substituted silicon atom pulls the neighboring iron atoms, whereas it pushes out the neighboring carbon atoms. In addition, the geometric distortions in $(Fe_{11}Si_{Fe}^{8d})C_4$ are significantly larger than in $(Fe_{11}Si_{Fe}^{4c})C_4$ case.

The calculated shortest interatomic distances from Al atom to Fe(8d), Fe(4c) and C(4c) atom are changed to 2.505Å, 2.739Å and 1.990Å in $(Fe_{11}Al_{Fe}^{4c})C_4$, respectively, which shows 0.4% and 1.6% expansion of the distance from Fe(4c) and Fe(8d), while the distance from C(4c) is contracted about 1.3% compared with Fe_3C. The tendency of $(Fe_{11}Al_{Fe}^{4c})C_4$ is almost opposite to the $(Fe_{11}Si_{Fe}^{4c})C_4$ case. The shortest interatomic distances of Fe(8d), Fe(4c) and

C(4c) measured from Fe(8d) atom are changed to 2.473Å, 2.494Å and 2.170Å in $(Fe_{11}Al^{8d}_{Fe})C_4$. This feature means that the interatomic distance from Fe(8d) to Fe(8d) , Fe(4c) and C(4c) are 0.8% expansion, 0.1% contraction and 7.8% expansion by Al substitution, respectively.

In the case of $(Fe_{11}Mn^{4c}_{Fe})C_4$, the shortest interatomic distances from Mn atom to Fe(8d), Fe(4c) and C(4c) atom are 2.495Å, 2.688Å and 2.014Å, respectively. This shows the slight contraction of the distance from both of three atoms. The calculated shortest interatomic distances from Mn atom to Fe(8d), Fe(4c) and C(4c) atom are changed to 2.470Å, 2.484Å and 2.000Å in $(Fe_{11}Mn^{8d}_{Fe})C_4$, respectively. In other words, the interatomic distance of Fe(8d) measured from Mn atom are expanded 0.7% while the distances from Fe(4c) and C(4c) are contracted 0.4% and 0.5%, respectively. These features show that the geometry distortion effect of Mn substitution is relatively small than those of Al and Si substitution case at both of Fe(4c) and Fe(8d) sites.

Type	x	Y	z	d(4c)	d(8d)
Fe(8d)	0.1752	0.0662	0.3330	2.625	0.000
Fe(8d)	0.1752	0.4338	0.3330	2.625	2.452
Fe(8d)	−0.1752	−0.0662	−0.3330	2.495	3.594
Fe(8d)	−0.1752	−0.4338	−0.3330	4.753	4.823
Fe(8d)	0.3248	−0.0662	−0.1670	2.581	2.526
Fe(8d)	0.3248	−0.4338	−0.1670	4.799	4.090
Fe(8d)	−0.3248	0.0662	0.1670	2.662	2.677
Fe(8d)	−0.3248	0.4338	0.1670	2.662	3.631
Fe(4c)	0.0358	0.2500	−0.1602	0.000	2.625
Fe(4c)	−0.0358	−0.2500	0.2602	3.650	2.495
Fe(4c)	0.4642	−0.2500	0.3398	4.582	2.581
Fe(4c)	−0.4642	0.2500	−0.3398	2.695	4.625
C(4c)	0.1236	−0.2500	−0.4379	3.589	4.053
C(4c)	−0.1236	0.2500	0.4379	2.800	2.021
C(4c)	0.3764	0.2500	0.0621	2.015	2.011
C(4c)	−0.3764	−0.2500	−0.0621	3.977	3.953

Table 3.2: Calculated atomic positions (in fractional units) of Fe_3C. d(4c) and d(8d) are the calculated interatomic distances in units of Å measured from one of the Fe(4c) and Fe(8d) atoms.

.

	x	y	z	d(Si)
Fe(8d)	0.1780	0.0673	0.3382	2.644
Fe(8d)	0.1780	0.4327	0.3382	2.644
Fe(8d)	−0.1726	−0.0644	−0.3298	2.466
Fe(8d)	−0.1726	−0.4356	−0.3298	4.754
Fe(8d)	0.3201	−0.0646	−0.1638	2.575
Fe(8d)	0.3201	−0.4354	−0.1638	2.575
Fe(8d)	−0.3214	0.0667	0.1583	2.601
Fe(8d)	−0.3214	0.4333	0.1583	2.601
Si(4c)	0.0301	0.2500	−0.1578	0.000
Fe(4c)	−0.0368	−0.2500	0.1624	3.647
Fe(4c)	0.4682	−0.2500	0.3424	4.607
Fe(4c)	−0.4627	0.2500	−0.3442	2.669
C(4c)	0.1241	−0.2500	−0.4374	3.596
C(4c)	−0.1326	0.2500	0.4290	2.757
C(4c)	0.3818	0.2500	0.0630	2.061
C(4c)	−0.3799	−0.2500	−0.0665	3.968

Table 3.3: Calculated atomic positions (in fractional units) of $(Fe_{11}Si_{Fe}^{4c})C_4$. d(Si) is the inteatomic distance in units of Å measured from the Si(4c) atom which replaces Fe(4c).

	x	y	z	d(Si)
Si(8d)	0.1987	0.0627	0.3391	0.000
Fe(8d)	0.1725	0.4250	0.3314	2.421
Fe(8d)	−0.1737	−0.0727	−0.3353	3.688
Fe(8d)	−0.1181	−0.4391	−0.3320	4.904
Fe(8d)	0.3207	−0.0713	−0.1627	2.498
Fe(8d)	0.3262	−0.4375	−0.1628	4.076
Fe(8d)	−0.3192	0.0738	0.1613	2.781
Fe(8d)	−0.3233	0.4318	0.1630	3.772
Fe(4c)	0.0408	0.2432	−0.1683	2.696
Fe(4c)	−0.0326	−0.2402	0.1684	2.466
Fe(4c)	0.4587	−0.2490	0.3443	2.473
Fe(4c)	−0.4729	0.2429	−0.3549	4.799
C(4c)	0.1196	−0.2739	−0.4255	4.114
C(4c)	−0.1414	0.2710	0.4484	2.287
C(4c)	0.3825	0.2758	0.0380	2.175
C(4c)	−0.3771	−0.2512	−0.0540	4.032

Table 3.4: Calculated atomic positions (in fractional units) of $(Fe_{11}Si_{Fe}^{8d})C_4$. d(Si) is the inteatomic distance in units of Å measured from the Si(8d) atom which replaces Fe(8d).

	x	y	z	d(Al)
Fe(8d)	0.1783	0.0667	0.3403	2.712
Fe(8d)	0.1783	0.4331	0.3403	2.625
Fe(8d)	−0.1771	−0.0674	−0.3344	2.505
Fe(8d)	−0.1771	−0.4326	−0.3344	4.761
Fe(8d)	0.3244	−0.0662	−0.1676	2.570
Fe(8d)	0.3244	−0.4338	−0.1676	4.786
Fe(8d)	−0.3278	0.0632	0.1636	2.680
Fe(8d)	−0.3278	0.4368	0.1636	2.705
Al(4c)	0.0268	0.2500	−0.1467	0.000
Fe(4c)	−0.0330	−0.2500	0.1589	3.670
Fe(4c)	0.4659	−0.2500	0.3414	4.617
Fe(4c)	−0.4583	0.2500	−0.3414	2.739
C(4c)	0.1239	−0.2500	−0.4370	3.605
C(4c)	−0.1300	0.2500	0.4163	2.909
C(4c)	0.3880	0.2500	0.0672	1.990
C(4c)	−0.3778	−0.2500	−0.0623	4.119

Table 3.5: Calculated atomic positions (in fractional units) of $(Fe_{11}Al^{4c}_{Fe})C_4$. d(Al) is the inteatomic distance in units of Å measured from the Al(4c) atom which replaces Fe(4c).

	x	y	z	d(Al)
Al(8d)	0.1871	0.0594	0.3403	0.000
Fe(8d)	0.1742	0.4297	0.3281	2.470
Fe(8d)	−0.1788	−0.0685	−0.3297	3.590
Fe(8d)	−0.1772	−0.4359	−0.3340	4.814
Fe(8d)	0.3256	−0.0688	−0.1597	2.528
Fe(8d)	0.3249	−0.4350	−0.1668	4.084
Fe(8d)	−0.3213	0.0690	0.1658	2.677
Fe(8d)	−0.3230	0.4371	0.1618	3.634
Fe(4c)	0.0422	0.2483	−0.1695	2.632
Fe(4c)	−0.0355	−0.2506	0.1635	2.484
Fe(4c)	0.4634	−0.2549	0.3471	2.578
Fe(4c)	−0.4672	0.2499	−0.3471	4.626
C(4c)	0.1218	−0.2594	−0.4285	4.036
C(4c)	−0.1371	0.2662	0.4462	2.010
C(4c)	0.3809	0.2682	0.0430	2.000
C(4c)	−0.3779	−0.2530	−0.4040	4.947

Table 3.6: Calculated atomic positions (in fractional units) of $(Fe_{11}Al^{8d}_{Fe})C_4$. d(Al) is the inteatomic distance in units of Å measured from the Al(8d) atom which replaces Fe(8d).

	x	y	z	d(Mn)
Fe(8d)	0.1762	0.0625	0.3347	2.620
Fe(8d)	0.1762	0.4347	0.3347	2.620
Fe(8d)	−0.1746	−0.0662	−0.3328	2.495
Fe(8d)	−0.1746	−0.4338	−0.3328	4.753
Fe(8d)	0.3248	−0.0660	−0.1672	2.590
Fe(8d)	0.3248	−0.4340	−0.1672	4.805
Fe(8d)	−0.3258	0.0654	0.1665	2.642
Fe(8d)	−0.3258	0.4346	0.1665	2.642
Mn(4c)	0.0325	0.2500	−0.1545	0.000
Fe(4c)	−0.0355	−0.2500	0.1597	3.638
Fe(4c)	0.4656	−0.2500	0.3402	4.583
Fe(4c)	−0.4639	0.2500	−0.3419	2.688
C(4c)	0.1230	−0.2500	−0.4368	3.598
C(4c)	−0.1232	0.2500	0.4351	2.759
C(4c)	0.3765	0.2500	0.0605	2.014
C(4c)	−0.3765	−0.2500	−0.0643	3.965

Table 3.7: Calculated atomic positions (in fractional units) of $(Fe_{11}Mn^{4c}_{Fe})C_4$. d(Mn) is the inteatomic distance in units of Å measured from the Mn(4c) atom which replaces Fe(4c).

	x	y	z	d(Mn)
Mn(8d)	0.1749	0.0646	0.3332	0.000
Fe(8d)	0.1750	0.4347	0.3315	2.470
Fe(8d)	−0.1776	−0.0653	−0.3312	3.590
Fe(8d)	−0.1742	−0.4333	−0.3334	4.814
Fe(8d)	0.3251	−0.0670	−0.1673	2.528
Fe(8d)	0.3246	−0.4334	−0.1685	4.084
Fe(8d)	−0.3251	0.0763	0.1680	2.677
Fe(8d)	−0.3243	0.4335	0.1669	3.634
Fe(4c)	0.0359	0.2510	−0.1597	2.632
Fe(4c)	−0.0360	−0.2495	0.1603	2.484
Fe(4c)	0.4653	−0.2503	0.3385	2.578
Fe(4c)	−0.4642	0.2504	−0.3388	4.626
C(4c)	0.1239	−0.2458	−0.4384	4.036
C(4c)	−0.1226	0.2467	0.4376	2.009
C(4c)	0.3757	0.2467	0.0636	2.000
C(4c)	−0.3761	−0.2501	−0.0623	3.947

Table 3.8: Calculated atomic positions (in fractional units) of $(Fe_{11}Mn_{Fe}^{8d})C_4$. d(Mn) is the inteatomic distance in units of Å measured from the Mn(8d) atom which replaces Fe(8d).

3.3 The Formation Energy

The Gibbs free energy is determined by the contribution of internal energy, work and entropy term. The changes of internal energy are calculated by formation energies. The formation energies were calculated as differences between the total energy of each phase and the sum of the energies of the stable state of pure elements forming this phase. The calculated total energies of the pure elements are summarized in Table 3.9. The formation energy (ΔU) of each system is defined, with the integers l, m and n, at zero Kelvin, as follows:

$$\Delta U = E(\mathrm{Fe}_l\mathrm{M}_m\mathrm{C}_n) - l \times E(\mathrm{Fe}) - m \times E(\mathrm{M}) - n \times E(\mathrm{C}), \qquad (3.1)$$

where $E(\mathrm{Fe}_l\mathrm{M}_m\mathrm{C}_n)$, $E(\mathrm{Fe})$, $E(\mathrm{Si})$, $E(\mathrm{Al})$, $E(\mathrm{Mn})$, and $E(\mathrm{C})$ are the total energies of $\mathrm{Fe}_l\mathrm{M}_m\mathrm{C}_n$, ferromagnetic BCC iron, diamond silicon, FCC aluminum, FCC manganese and graphite carbon, respectively, at the corresponding equilibrium lattice constants.

Table 3.10 gives the corresponding equilibrium lattice volumes, the formation energies and calculated bulk moduli of Fe_3C, $(Fe_{11}\,Si_{Fe}^{4c})C_4$, $(Fe_{11}Si_{Fe}^{8d})C_4$, $(Fe_{11}Al_{Fe}^{4c})C_4$, $(Fe_{11}Al_{Fe}^{8d})C_4$, $(Fe_{11}Mn_{Fe}^{4c})C_4$ and $(Fe_{11}Mn_{Fe}^{8d})C_4$ for ferromagnetic states, respectively. Substitution of Si and Mn leads to slightly smaller cell volumes than pure Fe_3C, while Al substitution induced bigger cell volumes. The calculated formation energy results show that Fe(8d) position replacements are more stable than Fe(4c) position for Si, Al and Mn alloying.

The formation energy of Fe_3C per formula unit is calculated to be about 21.5 kJ mol^{-1} which is only 3.2 kJ mol^{-1} larger than the experimental value, 18.3 kJ mol^{-1} (Miyamoto *et al.*, 2007). The formation energy of Fe_3C for a

unit cell is 86.1 kJ mol^{-1}, which is four times of 21.5 kJ mol^{-1}, to compare with substituted structures since one unit cell contains four formula units. The formation energies of $(Fe_{11}Si_{Fe}^{4c})C_4$ and $(Fe_{11}Si_{Fe}^{8d})C_4$ are calculated to 138.1 kJ mol^{-1} and 123.2 kJ mol^{-1}, respectively, which are 52.0 kJ mol^{-1} and 37.1 kJ mol^{-1} larger than the formation energy of four formula units of Fe_3C. It follows that 4.07 wt% silicon dissolved in a mole of cementite at zero Kelvin, requires 4.3 kJ for the Fe(4c) substitution and 3.1 kJ for the Fe(8d) substitution more energy than that required to form cementite using a mole of iron. It clearly is more difficult to form $(Fe_{11}Si_{Fe}^{4c})C_4$ and $(Fe_{11}Si_{Fe}^{8d})C_4$ than a mechanical mixture of Fe_3C and Si.

The formation energies of $(Fe_{11}Al_{Fe}^{4c})C_4$ and $(Fe_{11}Al_{Fe}^{8d})C_4$ are calculated to 76.1 kJ mol^{-1} and 72.5 kJ mol^{-1}, respectively, which are 10.0 kJ mol^{-1} and 13.6 kJ mol^{-1} smaller than that of Fe_3C unit cell. For one mole of iron, 3.92 wt% of aluminum solution at zero Kelvin, release 0.83 kJ for Fe(4c) substitution and 1.13 kJ for Fe(8d) substitution than required energy for cementite. The result is in disagreement with experimental observation that the solubility of aluminum in cementite is almost zero (Leslie, 1977) and with the MTDATA calculation results in Fig. 1.5. It is not at the moment clear why this discrepancy exists since there do not seem to be any adjustable parameters in the first principles calculations.

The formation energy of $(Fe_{11}Mn_{Fe}^{4c})C_4$ and $(Fe_{11}Mn_{Fe}^{8d})C_4$ are calculated to 81.7 kJ mol^{-1} and 81.1 kJ mol^{-1}, respectively, which are 4.4 kJ mol^{-1} and 5.0 kJ mol^{-1} smaller than that of Fe_3C unit cell. It means that 7.67 wt% manganese solution in a mole of cementite at zero Kelvin, release 0.37 kJ and 0.42 kJ for Fe(4c) and Fe(8d) position substitution, respectively, and it is matched well the experimental observation that Mn can dissolve easily in cementite (Leslie, 1977).

element	volume(Å^3)	V/ V_0	energy / kJ mol^{-1}	bulk modulus / GPa	
				calculation	measure
BCC Fe	11.36	0.97	−3340575.03	185.20	170
graphite C	8.89	1.01	−99997.13	37.69	33
diamond C	5.67	1.00	−99990.08	467.81	442
diamond Si	20.46	0.99	−761219.33	88.52	100
FCC Al	16.49	0.99	−637304.93	77.57	76
BCC Mn	10.87	0.89	−3040972.35	283.72	120
FCC Mn	10.96	0.90	−3040979.39	292.23	

Table 3.9: Calculated equilibrium atomic volumes, total energies, and bulk moduli of the reference materials of ferromagnetic BCC Fe, graphite C, diamond C, diamond Si, FCC Al, BCC Mn and FCC Mn. The experimental bulk moduli of the pure elements as included for reference, V_0 is the experimental volumes per atom of the reference elements (http://www.webelements.com).

type	volume(Å^3)	V/ V_0	ΔU \ kJ mol^{-1}	bulk modulus\ GPa
Fe_3C	152.20	0.980	21.5(86.1)	226.84
$(Fe_{11}Si^{4c})C_4$	151.44	0.975	138.1	221.83
$(Fe_{11}Si^{8d})C_4$	151.97	0.978	123.2	221.00
$(Fe_{11}Al^{4c})C_4$	152.48	0.982	76.1	224.02
$(Fe_{11}Al^{8d})C_4$	154.33	0.994	72.5	222.60
$(Fe_{11}Mn^{4c})C_4$	152.10	0.979	81.7	236.94
$(Fe_{11}Mn^{8d})C_4$	151.96	0.978	81.1	234.33

Table 3.10: Equilibrium unit cell volume, formation energy, and bulk moduli in ferromagnetic cases, which are calculated using the third order polynomial fitting with V_0 = 155.32 Å^3, the experimental volume of Fe_3C. The energy is stated in units of kJ mol^{-1} of each formula unit, Fe_3C has also the formation energy which is multiplied by four in parentheses to compare with $(Fe_{11}M^{4c}_{Fe})C_4$ and $(Fe_{11}M^{8d}_{Fe})C_4$. The reference states are ferromagnetic BCC Fe, graphite C, diamond Si, FCC Al and FCC Mn.

Table 3.11 contains the calculated results of equilibrium lattice parameters and internal coordinate of Si_3C, Al_3C and Mn_3C, which are composed of silicon, aluminum and manganese atoms by replacing all the iron atoms in cementite. Compared to those values of Fe_3C, the b-axis of Si_3C and Al_3C enlarge much, so the total volume becomes about 208 Å^3, which are about 34 % larger volume than that of Fe_3C. However the equilibrium volume of Mn_3C is about 3% smaller than Fe_3C.

Table 3.12 shows the equilibrium unit cell volume, formation energy per formula unit and the bulk moduli of the hypothetical Fe_3C, Si_3C, Al_3C and Mn_3C cementite. The calculated formation energies are 21.5 kJ mol^{-1}, 256.4 kJ mol^{-1}, 97.8 kJ mol^{-1} and -52.7 kJ mol^{-1} for its calculated equilibrium

lattice constants using the same optimization procedure with Fe_3C. The calculated excess energy of the Si_3C and Mn_3C over Fe_3C agree reasonably with 250 $kJ\,mol^{-1}$ and -40 $kJ\,mol^{-1}$ usually assumed in thermodynamic calculations (Miyamoto *el al*., 2007). The formation energy of Si_3C is one order larger than that of Fe_3C. When a silicon atom replaces an Fe atom in the ferromagnetic cementite, the required additional formation energy is 37.1 $kJ\,mol^{-1}$ and 52.0 $kJ\,mol^{-1}$ for the Fe(4c) sites. If this excess energy is scaled in proportion to the corresponding site occupation numbers of iron atoms substituted with silicon in the cementite unit cell, then 505.6 $kJ\,mol^{-1}$ can be obtained that is about half the value of the four formula unit of Si_3C. It follows that a simple analysis in terms of pair-wise Si-Fe binding energies is likely to be a gross approximation of the actual effect of silicon substitution. If the excess energies of aluminum and manganese substitution are scaled in proportion to the corresponding site occupation, then it can be obtained as -148.8 $kJ\,mol^{-1}$ and -37.6 $kJ\,mol^{-1}$. The value for manganese substitution matched well with -40 $kJ\,mol^{-1}$ which is usually used in thermodynamic calculations and the value of Mn_3C, but the results of aluminum substitution gave a large difference. The results of VASP also are contained in the Table3.12. The results of Fe_3C and Si_3C are well acceptable in certain range of precision with FLAPW results. The result of Mn_3C gives a gap with expected value since the VASP calculations do not treat core-valence interaction properly.

	Fe_3C	Si_3C	Al_3C	Mn_3C
a (Å)	5.1281	5.2745	5.3196	4.9914
b (Å)	6.6512	8.1651	7.8539	6.6721
c (Å)	4.4623	4.8365	4.9738	4.4321
volume($Å^3$)	152.20	208.29	207.80	147.60
x_1	0.1752	0.2514	0.1828	0.1861
x_2	0.0358	0.0109	0.0193	0.0308
x_3	0.1236	0.2454	0.2282	0.1225
y_1	0.0662	0.0327	0.0845	0.0650
z_1	0.1670	0.1896	0.1630	0.1572
z_2	0.1602	0.2558	0.1867	0.1553
z_3	0.0621	0.0588	0.0994	0.0646

Table 3.11: Calculated equilibrium lattice parameters in units of Å and internal coordinate in fractional units of the hypothetical M_3C with the fully optimized structure. The calculated values of the Fe_3C cementite crystal structure are included for reference.

type	volume(Å^3)	V/ V_0	ΔU(kJ mol^{-1}) VASP	FLAPW	Bulk modulus / GPa
Fe_3C (FM)	152.20	0.980	18.8	21.5	226.84
Si_3C (NM)	208.29	1.341	260.0	256.4	130.90
Al_3C (NM)	207.80	1.338	58.0	97.8	94.76
Mn_3C (NM)	147.60	0.950	−26.7	−52.7	329.34

Table 3.12: Equilibrium unit cell volume, formation energy, and bulk moduli which are calculated using the third order polynomial fitting with V_0 = 155.32 Å^3, the experimental volume of Fe_3C. The energy is stated in units of kJ mol^{-1} of each formula unit. Only Fe_3C is ferromagnetic state but the others are nonmagnetic cases. The formation energy from VASP are from Miyamoto's paper (Miyamoto, 2007). The referenced states are ferromagnetic BCC Fe, graphite C, diamond Si, FCC Al and FCC Mn.

Fig. 3.2 shows the dependency of formation energy at zero Kelvin with respect to silicon, aluminum and manganese atomic concentration in cementite for the ferromagnetic Fe_3C, $(Fe_{11}Si^{4c}_{Fe})C_4$, $(Fe_{11}Si^{8d}_{Fe})C_4$, $(Fe_{11}Al^{4c}_{Fe})C_4$, $(Fe_{11}Al^{8d}_{Fe})C_4$, $(Fe_{11}Mn^{4c}_{Fe})C_4$, $(Fe_{11}Mn^{8d}_{Fe})C_4$ and nonmagnetic Si_3C, Al_3C, Mn_3C. It is clear to see that the formation energy behavior is nonlinear to the alloying concentrations in cementite. Figs. 3.3, 3.4 and 3.5 show the equilibrium ternary phase diagrams of Fe-Si-C, Fe-Al-C and Fe-Mn-C at 773K, respectively, using MTDATA, with TCFE database and FLAPW calculation results. A free energy of cementite phase has been modified as substitutional solid solution $(Fe, Si)_3C$, $(Fe, Al)_3C$ or $(Fe, Mn)_3C$ using the same effect of temperature dependency with Fe_3C and using the FLAPW results of Si_3C, Al_3C or Mn_3C. The excess energy term has been modified using a regular solution model and using the FLAPW results of $(Fe_{11}M)C_4$ without temperature dependency.

$$G^{ex} = \Omega\, X(1 - X). \tag{3.2}$$

These diagram results agree well with Figs. 1.4 and 1.5 at high Fe and at low Si, Al and Mn concentration. However, the details are unexpected, for example, the shape of the phase fields. These diagrams need further interpretation and detailed work, especially in the case of aluminum, where there appears to be a large solubility of aluminum in cementite, with a continuous transition from Fe_3C to Al_3C as if they are isomorphous carbides. This is probably inconsistent with experimental evidence.

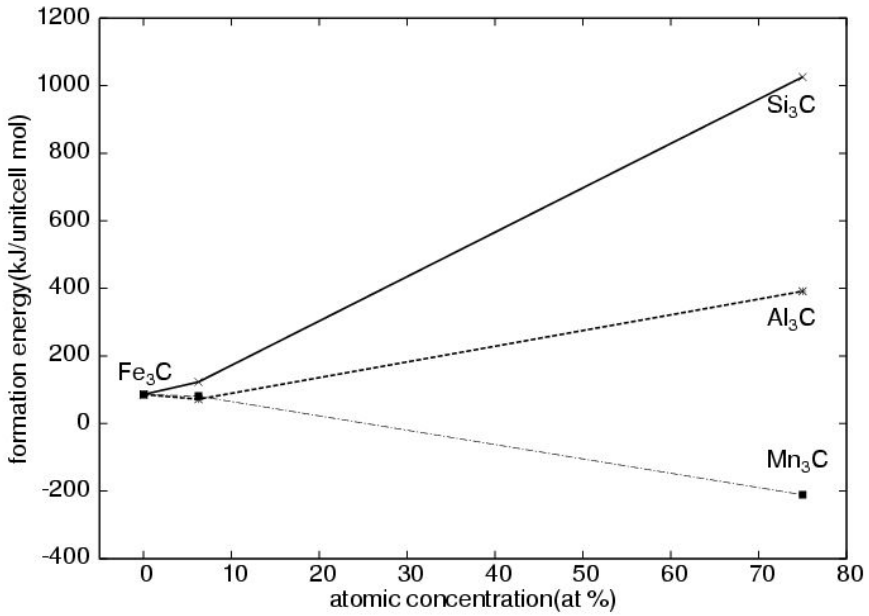

Figure 3.2 Calculated formation energy of one mole of unit cell with respect to alloying concentration (in units of at %) in Fe_3C cementite. The lines are drawn as a guides.

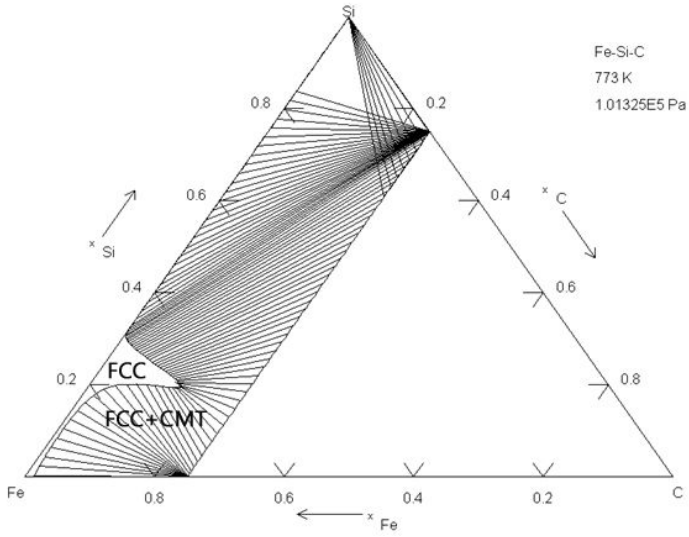

Figure 3.3 Ternary phase diagram of Fe-Si-C system at 773K using FLAPW calculation results.

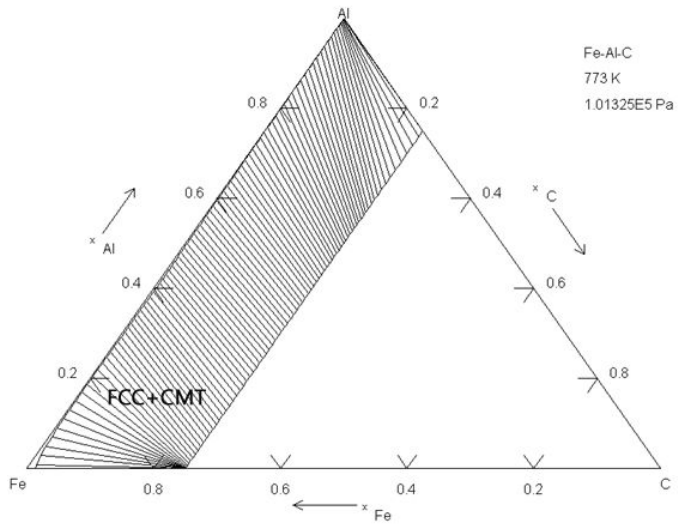

Figure 3.4 Ternary phase diagram of Fe-Al-C system at 773K using FLAPW calculation results.

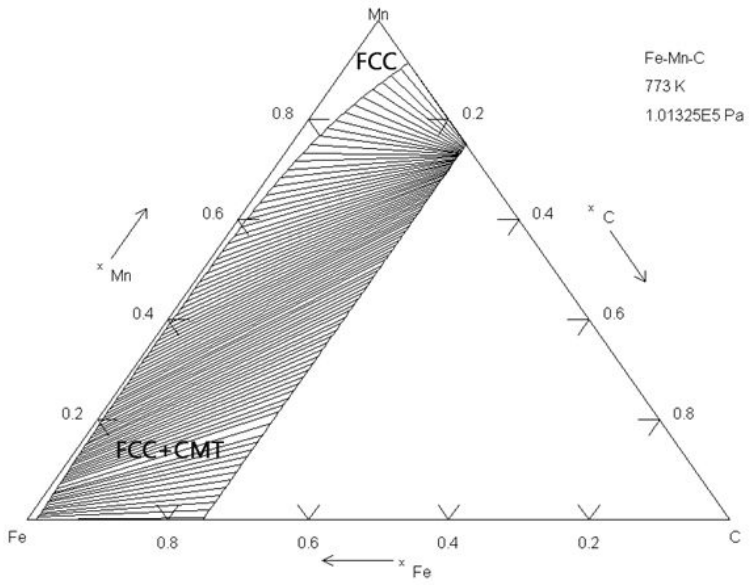

Figure 3.5 Ternary phase diagram of Fe-Mn-C system at 773K using FLAPW calculation results.

3.4 Bulk Moduli

Table 3.9 contains also the bulk moduli of pure elements for the reference state of system. The bulk modulus can be obtained from the fitting coefficients of Murnaghan's equation (Murnaghan, 1944) or from the partial derivative of pressure (Ashcroft, 1976),

$$P = -(\frac{\partial E}{\partial V}) \tag{3.3}$$

$$B = -V(\frac{\partial P}{\partial V}). \tag{3.4}$$

The bulk modulus of three dimensional symmetric crystal structure such as BCC, FCC and diamond are calculated using the third order total energy

polynomial depend on lattice volume. But graphite carbon is hexagonal and the elastic modulus in c-direction is significantly smaller compared with the other axes. So the bulk modulus of hexagonal graphite should be calculated using elastic constants (Boettger, 1997) by using the equations

$$C_{11} + C_{12} = \frac{{a_0}^2}{2V_0}\frac{\delta^2 E}{\delta a^2} \tag{3.5}$$

$$C_{33} = \frac{{c_0}^2}{2V_0}\frac{\delta^2 E}{\delta c^2} \tag{3.6}$$

$$C_{13} = \frac{a_0 c_0}{2V_0}\frac{\delta^2 E}{\delta a\, \delta c} \tag{3.7}$$

$$\mathrm{B} = \frac{C_{33}(C_{11}+C_{12})-2{C_{13}}^2}{(C_{11}+C_{12})+2C_{33}-4C_{13}}. \tag{3.8}$$

where V_0, a_0 and c_0 are the equilibrium value of volume and lattice parameter a and c. The 25 distinct combinations of the hexagonal lattice parameters a and c are used to determine a second order two dimensional fitting polynomial for graphite internal energy. The elastic constants ($C_{11} + C_{12}$), C_{33} and C_{13} and bulk modulus of graphitic carbon are calculated to be 1248.3 GPa, 40.9 GPa, -5.7 GPa and 37.69 GPa, respectively. The calculated bulk moduli for pure elements are agreed well with the known value except manganese case such as in Table 3.9. This comes from the fact that BCC and FCC structures are not equilibrium crystal structures of manganese in which the alpha structure is most stable.

Table 3.10 contains the bulk moduli of Fe_3C, $(Fe_{11}Si^{4c}_{Fe})C_4$, $(Fe_{11}Si^{8d}_{Fe})C_4$, $(Fe_{11}Al^{4c}_{Fe})C_4$, $(Fe_{11}Al^{8d}_{Fe})C_4$, $(Fe_{11}Mn^{4c}_{Fe})C_4$ and $(Fe_{11}Mn^{8d}_{Fe})C_4$. The calculated bulk modus of ferromagnetic Fe_3C is 226.84 GPa which is agrees reasonably with the previous first-principles result of 235.13 GPa (Faraoun *et al*., 2006). The small discrepancy is attributed to the different precision criteria they used. The substitution of Si into the Fe(4c) site and Fe(8d) sites reduces the bulk

moduli about 2.2% and 2.6%, respectively. The corresponding reductions in the aluminum substitution are about 1.3% for the Fe(4c) substitution and 1.9% for the Fe(8d) substitution. These features indicate that the Si and Al substation at Fe(8d) positions lead to a larger reduction in the bulk modulus than that at the Fe(4c) positions. The bulk moduli of $(Fe_{11}Mn_{Fe}^{4c})C_4$ and $(Fe_{11}Mn_{Fe}^{8d})C_4$ are 4.5% and 3.3% higher than Fe_3C. For the three alloying elements substitutions, replacements at Fe(4c) positions gives higher bulk moduli than at Fe(8d) positions.

Table 3.12 shows the calculated bulk moduli of nonmagnetic Si_3C, Al_3C, and Mn_3C. The tendency of bulk moduli increasing is the same as the alloying elements substitution described above such that silicon and aluminum decreased while manganese increased. However the bulk modulus of Si_3C is higher than Al_3C, which is different from the result that $(Fe_{11}Si_{Fe}^{4c})C_4$, $(Fe_{11}Si_{Fe}^{8d})C_4$ are smaller than $(Fe_{11}Al_{Fe}^{4c})C_4$, $(Fe_{11}Al_{Fe}^{8d})C_4$.

3.5 Magnetic Properties

Table 3.13 summarizes the calculated total magnetic moments, in units of μ_B, which are $5.764\mu_B$, $4.907\mu_B$, $4.767\mu_B$, $4.729\mu_B$, $4.856\mu_B$, $5.654\mu_B$ and $5.577\mu_B$ for Fe_3C, $(Fe_{11}Si_{Fe}^{4c})C_4$, $(Fe_{11}Si_{Fe}^{8d})C_4$, $(Fe_{11}Al_{Fe}^{4c})C_4$, $(Fe_{11}Al_{Fe}^{8d})C_4$, $(Fe_{11}Mn_{Fe}^{4c})C_4$ and $(Fe_{11}Mn_{Fe}^{8d})C_4$, respectively. This shows Si and Al substitution reduced the total magnetic moments while Mn substitution increased. For Fe_3C, the calculated spin magnetic moment inside the MT spheres of Fe(8d) and Fe(4c) are $2.059\mu_B$ and $1.957\mu_B$, respectively. On the other hand, the carbon atom spins are polarized negatively to have the magnetic moment of $-0.089\mu_B$ and the interstitial regions have a magnetic moment of $-0.120\mu_B$.

The substitution of Si and Al reduced the total magnetic moments by reducing the spin magnetic moments in Fe(4c) and Fe(8d) muffin-tin sphere while the spin magnetic moments in C(4c) and interstitial are increased. The Al and Si substitution at Fe(8d) positions reduced more the magnetic moment at Fe(4c) while it is opposite tendency at Fe(8d). The substitution of Mn reduced the total magnetic moments less than is the case for Si and Al. The change of spin magnetic moments at each muffin-tin sphere is also relatively small.

Fig. 3.6 presents the spin density contour plots in the plane normal to the b-axis intersect the Fe(4c) positions, whereas Fig. 3.7 intersect the Fe(8d) positions for Fe_3C, $(Fe_{11}Mn_{Fe}^{4c})C_4$, $(Fe_{11}Si_{Fe}^{4c})C_4$ and $(Fe_{11}Al_{Fe}^{4c})C_4$. The contours start from 1.0×10^{-3} electrons/a. u.^{3} and increase successively by a factor of $\sqrt{2}$. The solid and broken lines represent the positively and negatively polarized spins, respectively. Fig. 3.8 presents the spin density contour plots in the plane which contains Fe(4c), C(4c), and Fe(8d) sites simultaneously for Fe_3C, $(Fe_{11}Mn_{Fe}^{8d})C_4$, $(Fe_{11}Si_{Fe}^{8d})C_4$ and $(Fe_{11}Al_{Fe}^{8d})C_4$.

The Mn substitution on one Fe(4c) and Fe(8d) site has relatively small effect on the spin density compared with Si and Al substitution. Fe(4c)-d and Mn(4c)-d bonding is more stronger than Fe(4c)-d and Fe(4c)-d bonding, so positively charged region surrounding Fe(4c) sites are expanded. The most significant difference is come from the comparison with Si and Al substitution at Fe(4c) sites. The Si substitution on one Fe(4c) site replaces the bonding between the Fe-d and the C-sp states by that of the Si-sp and C-sp. It is noticeable that the spins of the Si-C bonding region are polarized positively, while the Al substitution did not. In addition, the σ-like bonding between the Fe(4c)-d and the C(4c)-p shows enhanced negative spin polarizations, so the positively spin polarized region of Fe(4c) site is reduced. This indirect effect

of Si substitution is considered to cause the large reduction of the magnetic moment of Fe(4c) in $(Fe_{11}Si_{Fe}^{4c})C_4$.

The effects on the magnetism of the Si and Al substitution on the Fe(8d) site seems rather direct. The spins of the π-like bonding between Si(8d)-p and Fe(4c)-d and between Al(8d)-p and Fe(4c)-d are polarized negatively due to the Si and Al substitution. It is considered that the magnetic moment reduction on the Fe(4c) site by Si and Al substitution on Fe(8d) site is due to the direct effect of the π-like bonding between the Si(8d)-p and the Fe(4c)-d states and between Al(8d)-p and the Fe(4c)-d states.

In Figs. 3.9-3.11, it is presented the calculated atom projected local density of states (LDOS) for the (a) Fe(4c) and (b) Fe(8d) atoms for Fe_3C, $(Fe_{11}Si_{Fe}^{4c})C_4$, $(Fe_{11}Si_{Fe}^{8d})C_4$, $(Fe_{11}Al_{Fe}^{4c})C_4$, $(Fe_{11}Al_{Fe}^{8d})C_4$, $(Fe_{11}Mn_{Fe}^{4c})C_4$ and $(Fe_{11}Mn_{Fe}^{8d})C_4$, respectively. The spin down DOS values are factored by -1, and the Fermi levels (E_F) are set to zero. It can be found that all the Fe bands are broadened and split into sub-bands by the silicon and aluminum substitution, due to local symmetry breaking caused by the substitution while manganese substitution gives relatively small effect on the band. This feature is considered to the reason for the general reduction of Fe magnetic moments by the silicon and aluminum substitution.

	total	Fe(4c)	Fe(8d)	C(4c)	interstitial	M
Fe_3C	5.764	2.059	1.957	−0.089	−0.120	-
Fe_3C (LMTO)	-	1.980	1.740	−0.060	-	-
$(Fe_{11}Si^{4c})C_4$	4.907	2.021	1.793	−0.075	−0.107	−0.055
$(Fe_{11}Si^{8d})C_4$	4.767	1.881	1.852	−0.077	−0.259	−0.076
$(Fe_{11}Al^{4c})C_4$	4.729	1.913	1.752	−0.078	−0.118	−0.054
$(Fe_{11}Al^{8d})C_4$	4.856	1.890	1.805	−0.076	−0.103	−0.057
$(Fe_{11}Mn^{4c})C_4$	5.654	2.080	1.895	−0.089	−0.102	1.978
$(Fe_{11}Mn^{8d})C_4$	5.577	2.020	1.920	−0.088	−0.106	1.564

Table 3.13: Calculated magnetic moments per formula unit of Fe_3C, $(Fe_{11}M_{Fe}^{4c})C_4$ and $(Fe_{11}M_{Fe}^{8d})C_4$ those of each atom (in units of μ_B) inside each muffin-tin (MT) sphere and those of interstitial region. The LMTO calculation is referenced from the paper of Haglund (1991).

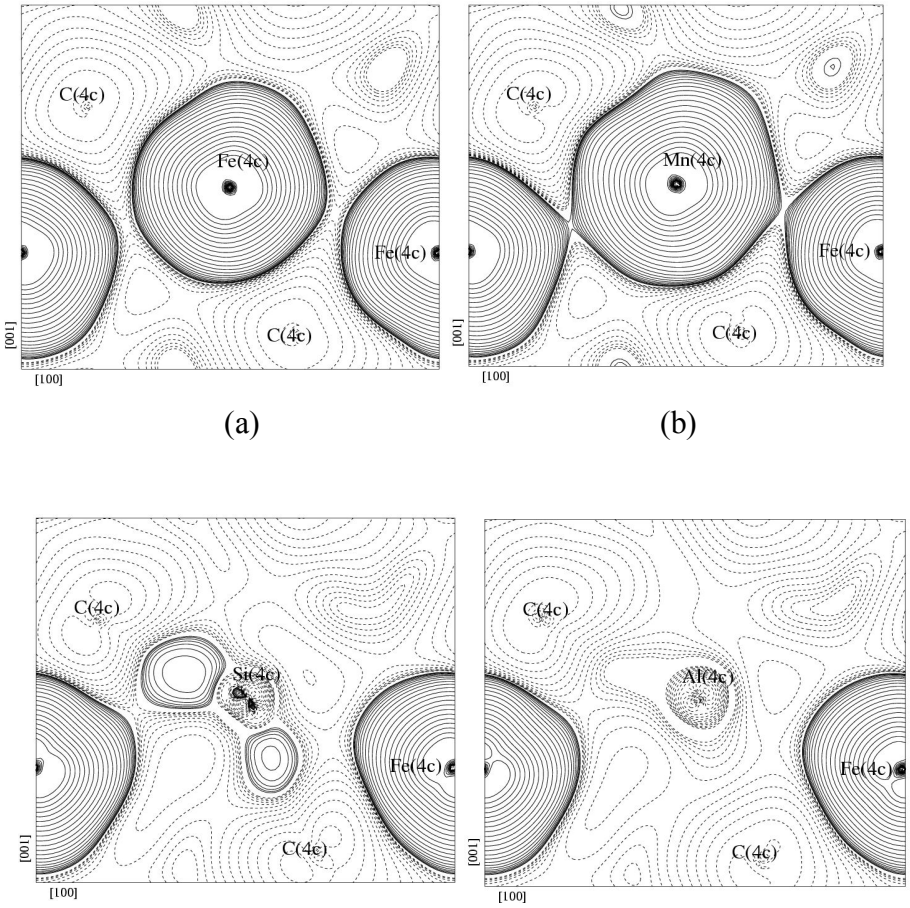

Figure 3.6 Spin density contour plots in the plane normal to the b-axis, cutting the Fe(4c) positions of (a) Fe_3C (b) $(Fe_{11}Mn_{Fe}^{4c})C_4$ (c) $(Fe_{11}Si_{Fe}^{4c})C_4$ (d) $(Fe_{11}Al_{Fe}^{4c})C_4$. The horizontal axis represents [100] direction, while the vertical axis represents [001] one. Contours start from 1.0×10^{-3} electrons/a.u.^{3} and increase successively by a factor of $\sqrt{2}$. The solid and broken lines represent the positively and negatively polarized spins, respectively.

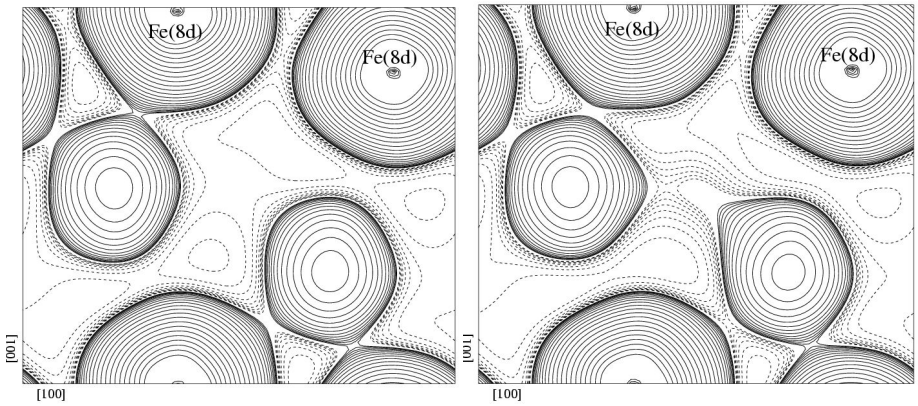

Figure 3.7 Spin density contour plots in the plane normal to the b-axis, cutting the Fe(8d) positions of (a) Fe_3C (b) $(Fe_{11}Mn_{Fe}^{4c})C_4$ (c) $(Fe_{11}Si_{Fe}^{4c})C_4$ (d) $(Fe_{11}Al_{Fe}^{4c})C_4$. The horizontal axis represents [100] direction, while the vertical axis represents [001] one. Contours start from 1.0×10^{-3} electrons/a.u.^{3} and increase successively by a factor of $\sqrt{2}$. The solid and broken lines represent the positively and negatively polarized spins, respectively.

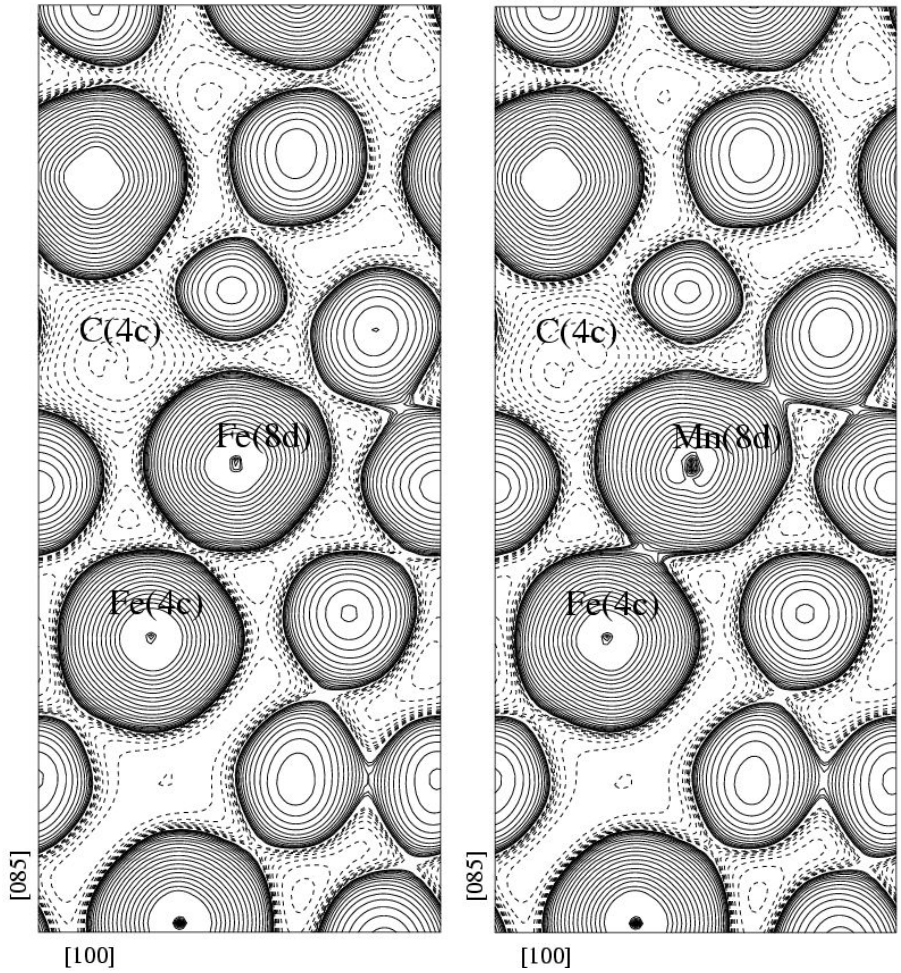

(a) (b)

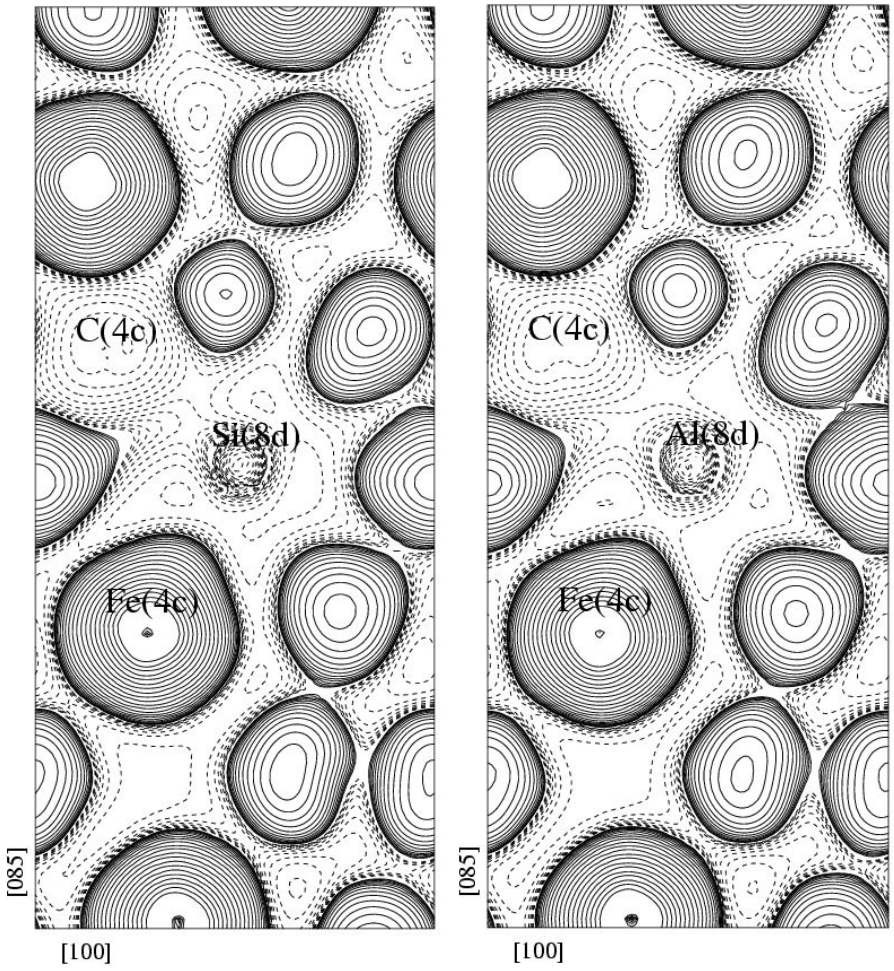

(c) (d)

Figure 3.8 Spin density contour plots in the plane which contains Fe(4c), C(4c) and Fe(8d) sites simultaneously for (a) Fe_3C (b) $(Fe_{11}Mn_{Fe}^{4c})C_4$ (c) $(Fe_{11}Si_{Fe}^{4c})C_4$ (d) $(Fe_{11}Al_{Fe}^{4c})C_4$. The horizontal axis represents [100] direction, while the vertical axis represents [085] one. Contours start from 1.0×10^{-3} electrons/a. u.^{3} and increase successively by a factor of $\sqrt{2}$. The solid and broken lines represent the positively and negatively polarized spins, respectively.

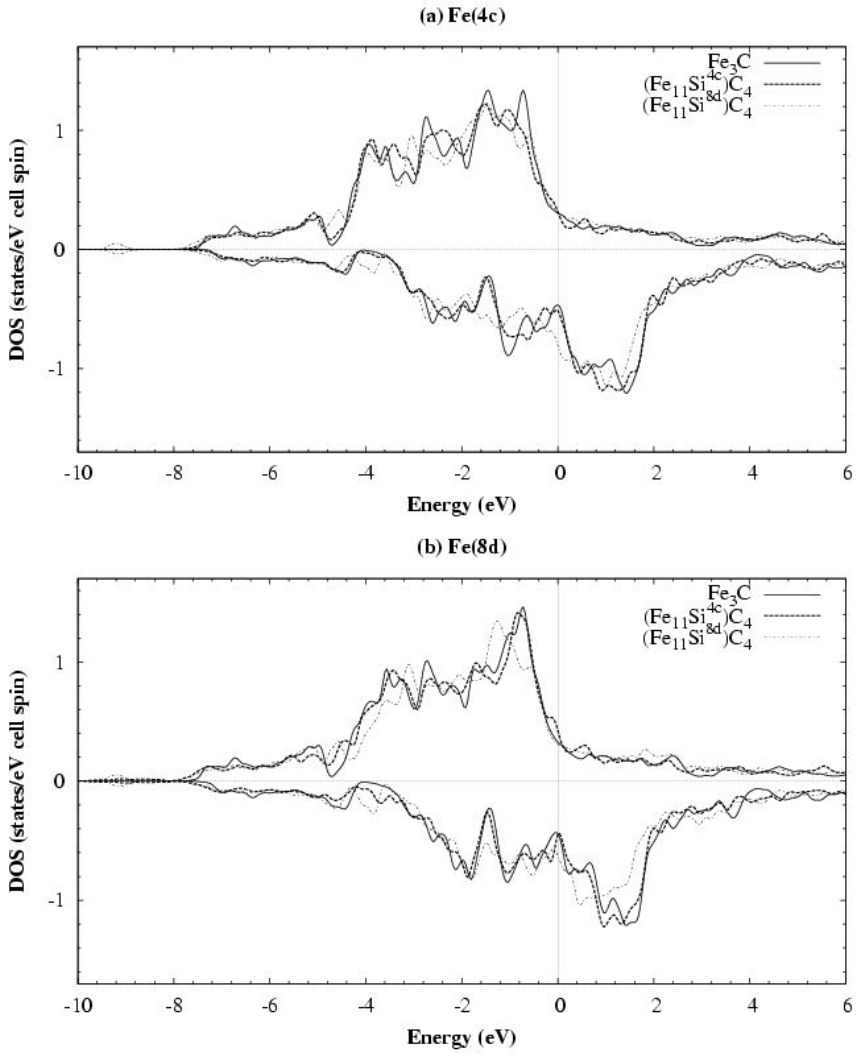

Figure 3.9 The calculated atom projected local density of states (LDOS) for the (a) Fe(4c) and (b) Fe(8d) atoms. The solid lines, broken lines, and dot-dashed lines represent the atoms belonging to Fe_3C, $(Fe_{11}Si_{Fe}^{4c})C_4$ and $(Fe_{11}Si_{Fe}^{8d})C_4$, respectively. The spin down DOS values are factored by -1, and the Fermi levels (E_F) are set to zero.

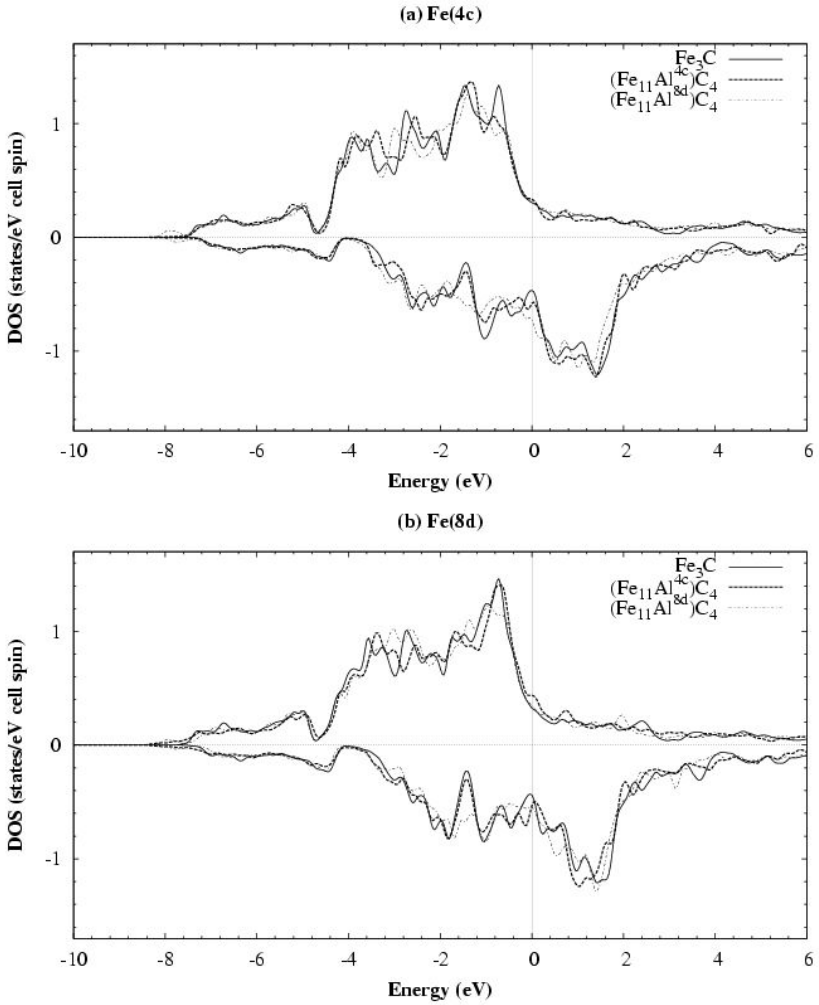

Figure 3.10 The calculated atom projected local density of states (LDOS) for the (a) Fe(4c) and (b) Fe(8d) atoms. The solid lines, broken lines, and dot-dashed lines represent the atoms belonging to Fe_3C, $(Fe_{11}Al^{4c}_{Fe})C_4$ and $(Fe_{11}Al^{8d}_{Fe})C_4$, respectively. The spin down DOS values are factored by -1, and the Fermi levels (E_F) are set to zero.

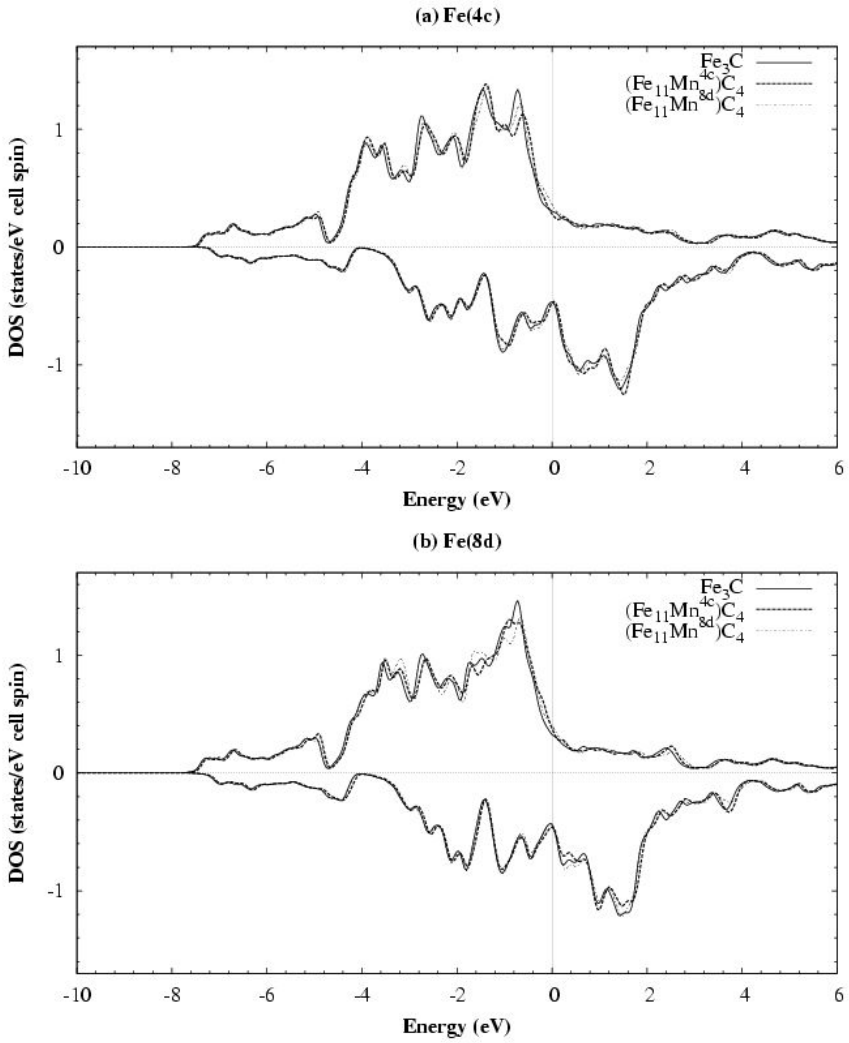

Figure 3.11 The calculated atom projected local density of states (LDOS) for the (a) Fe(4c) and (b) Fe(8d) atoms. The solid lines, broken lines, and dot-dashed lines represent the atoms belonging to Fe_3C, $(Fe_{11}Mn_{Fe}^{4c})C_4$ and $(Fe_{11}Mn_{Fe}^{8d})C_4$, respectively. The spin down DOS values are factored by -1, and the Fermi levels (E_F) are set to zero.

Ⅳ Conclusions

The electronic structures and magnetic properties of cementite and its corresponding silicon, aluminum and manganese substituted forms have been investigated using first-principles calculations based on the FLAPW method within GGA. In addition, those of hypothetical Si_3C, Al_3C and Mn_3C in the cementite crystal structure have been investigated by replacing the iron atoms with appropriate solute atoms. The calculated equilibrium volume of the ferromagnetic Fe_3C ground state agrees well (within 1.4%) with the experimental data extrapolated to zero Kelvin. The internal coordinate relaxations show that the substituted Si atom pulls the neighboring Fe atoms, while it pushes the neighboring carbon atoms. The substituted Si atom and substituted Al atom at Fe(8d) sites push the neighboring carbon atoms while the substituted Mn atom and substituted Al atom at Fe(4c) pulls them. The bulk modulus of Fe_3C is reduced a few percent on substitution of Si and Al and increased on substitution of Mn.

The total energy calculations indicate that the substitution of an individual silicon atom in cementite leads to an increase in the formation energy of pure cementite about 52.1 kJ mol^{-1} for the Fe(4c) substitutions or 37.2 kJ mol^{-1} for the Fe(8d) substitutions. The Al and Mn substitution lead to reductions in the formation energy of pure cementite by 10.0 kJ mol^{-1} and 4.4 kJ mol^{-1} for the Fe(4c) substitution or 13.6 kJ mol^{-1} and 5.0 kJ mol^{-1}, respectively. The corresponding excess energies when all the iron atoms are substituted to form Fe_3C, Si_3C, Al_3C and Mn_3C are 21.5 kJ mol^{-1}, 256.4 kJ mol^{-1}, 97.8 kJ mol^{-1} and -52.7 kJ mol^{-1}, respectively. The results can give a explanation of the experimental observation that Si are not soluble in cementite while Mn can be solved easily. However, the reduction of the formation energy for Al substitution needs more study to explain that it

contradicts with experimental observation.

It is found that on substitution of a manganese atom, the magnetic moment changes relatively small compared with those of a silicon atom and aluminum atom. The calculated spin density contour plots and the Fe(4c) projected atom projected local density of states reveal that the magnetic moment reduction at Fe(4c) site by the Si substitution at Fe(4c) site is indirect bonding through the neighboring carbon atom, whereas at the Fe(8d) site it is direct.

References

Allten, A. G., Payson, P., The Effect of Silicon on the Tempering of Martensite, *Trans. ASM*, 45:498-532, 1953

Ashcroft, N. W., Mermin, N. D., Solid State Physics, Brooks-cole, 1976

Bain, E. C., Alloying Elements in Steel, *American Society of Materials*, Cleveland, Ohio, USA, 1939

Bhadeshia, H. K. D. H., Edmonds, D. V., Bainite in silicon steels: new composition-property approach Part 1, *Metal Science*, 17:420-425, 1983

Bhadeshia, H. K. D. H., Advances in the kinetic theory of carbide precipitation, *Materials Science Forum*, 426-432, 2003

Bhadeshia, H. K. D. H., Lord, M., Svensson, L. E., Silicon-Rich Bainite Steel Welds, *Transactions of JWRI*, 32:43-52, 2003

Bhadeshia, H. K. D. H., Honeycombe, R. W. K., Steels: Microstructure and properties, Third edition, 2006

Blugel, S., Bihlmayer, G., Full-Potential Linearized Augmented Planewave Method, *Computational nanoscience: Do It Yourself*, 31:85-129, 2006

Caballero, F. G., Bhadeshia, H. K. D. H., Mawella, K. J. A., Jones, D. G. and Brown, P., Design of novel high strength bainitic steels, *Part1:Materials Science and Technology*, 17:512-516, 2001

Caballero, F. G., Bhadeshia, H. K. D. H., Mawella, K. J. A., Jones, D. G. and Brown, P., Design of novel high strength bainitic steels, *Part2:Materials Science and Technology*, 17:517-522, 2001

Caballero, F. G., Bhadeshia, H. K. D. H., Mawella, K. J. A., Jones, D. G. and Brown, P., Very strong low temperature bainite, *Materials Science and Technology*, 18:279-284, 2002

Caballero, F.G., Bhadeshia, H. K. D. H., Very strong bainite, *Current Opinion in Solid State and Materials Science*, 8:251-257, 2004

Callister, W. D., Materials Science and Engineering: An Introduction, Wiley, 2003

Chatterjee, S., Murugananth, M., Bhadeshia, H. K. D. H., δ-TRIP steel, *Materials Science and Technology*, 23:819-827, 2007

De Cooman, B., Structure-properties relationship in TRIP steels containing carbide-free bainite: *Current Opinion in Solid State and Materials Science*, 8:285-303, 2004

Deliry, J., A new iron carbide during bainitic transformation in silicon-carbon steels, *Memoires Scientifiques Rev. Metallurg.*, 62:527-550, 1965

Entin. R, The elementary reactions in the austenite-pearlite, bainite transformations: in *V. F. Zacky, H. I. Aaronson (Eds.), Decomposition of austenite by diffusional processes, Interscience, New York*, pp295-211, 1962

Faraoun, H. I., Zhang, Y. D., Esling, C., Aourag, H., Crystalline, electronic, and magnetic structures of θ-Fe_3C, χ-Fe_5C_2, η-Fe_2C from first principle calculations, *Journal of Applied Physics*, 99:093508, 2006

Fasiska, E. J., Jeffrey, G. A., On the cementite Structure, *Acta Crystallographica*, 19:463-471, 1965

Fock, V., *Z. Phys*, 26:126, 1930

Garcia-Mateo, C., Caballero, F. G., Bhadeshia, H. K. D. H., Development of hard bainite, *ISIJ International*, 43:1238-1243, 2003

Garcia-Mateo, C., Caballero, F. G., Bhadeshia, H. K. D. H., Acceleration of low temperature bainite, *ISIJ International*, 43:1821-1825, 2003

Ghosh, G., Olson, G. B., Precipitation of paraequilibrium cementite: Experiments, and thermodynamic and kinetic modeling, *Acta Materialia*, 50:2099-2119, 2002

Gordine, J., Codd, I., The influence of silicon up to 1.5 wt. percent on the tempering characteristics of a spring steel, *Journal of the Iron and Steel Institute*, 207:461-467, 1969

Haglund, J., Grimvall, G., Jarlborg, T., Electronic structure, X-ray photoemission spectra, and transport properties of Fe_3C (cementite), *Physical Review B*, 44:2914-2919, 1991

Hehemann, R. F., The bainite transformation, *H.I. Aaronson, V.F.Zackay (Eds.), Phase Transformations*, pp. 397-432, 1970

Herstein, F. H., Smuts, J., Comparison of X-ray and neutron-diffraction refinements of the structure of cementite Fe_3C, *Acta Crystallographica*, 17:1331-1332, 1964

Hilliard, J. E., Phase Transformations, *ASM*, 1970

Hwang, N. M., *et al.*, Thermodynamics and kinetics for nucleation of diamonds in the chemical vapor deposition process, *Diamond and Related Materials*, 1:191-194, 1992

Hwang, N. M., *et al.*, Simulation of the effect of anisotropic grain boundary mobility and energy on abnormal grain growth, *Journal of Material Science*, 33:5625-5629, 1998

Jacques, P. J., Transformation-induced plasticity for high strength formable steels, *Current Opinion in Solid State and Materials Science*, 8:259-265, 2004

Keh, A. S., Leslie, W. C., Structure and properties of engineering materials, *Materials Science Research, Vol.1: Plenum Publishing*, N. Y. USA, 1963

Koelling, D. D., Harmon, B. N., A technique for relativistic spin-polarised calculations, *Journal of Physics C*, 10:3107-3114, 1977

Kozeschnik, E., Bhadeshia, H. K. D. H., Influence of silicon on cementite precipitation in steels, *Materials Science and Technology*, 24, doi:10.1179/174328408X275973, 2008

Lee, B. J., Numerical procedure for simulation of Multicomponent and Multi-Layered Phase Diffusion, *Metals and Materials*, 5:1-15, 1999

Lee, B. J., Prediction of the Amount of Retained delta-ferrite and Microsegregation in an Austenitic Stainless Steel, Z. Metallkunde, 90:522-530 (1999)

Lee, H. S., First-Principles study of defect energetic in $BaTiO_3$, 2006

Le-Houillier, R., Begin, G., Dube, A., A study of the peculiarities of austenite during the bainite transformation, *Matallurgical Transactions*, 2:2645-2653, 1971

Leslie, W. C., Rauch, G. C., Precipitation of carbide in low-carbon Fe-Al-C alloys, *Metallurgical and Materials Transactions A*, 8:1073-5623, 1977

Lorimer, G. W., Hobbs, R. M., Ridley, N., Effect of Si on the Microstructure

of quenched and tempered medium-C steels, *Journal of the Iron and Steel Institute*, 210:757-764, 1972

Matas, S. J., Hehemann, R. F., The structure of bainite in hypoeutectoid steels, *TMS-AIME*, 221:179-185, 1961

Matsumura, O., Sakuma, Y., Takechi, H., Enhancement of elongation by retained austenite in intercritically annealed 0.4C-1.5Si-0.8Mn Steel, *Transactions of the Iron and Steel Institute of Japan*, 27:570-579, 1987

Matsumura, O., Sakuma, Y., Takechi, H., TRIP and its kinetic aspects in austempered 0.4C-1.5Si-0.8Mn steel, *Scripta Metallurgica*, 27:1301-1306, 1987

Medvedeva, N. I., Kar'kina, L. E., Ivanovskii, A. L., Effect of chromium on the electronic structure of the cementite Fe_3C, *Physics of the Solid State*, 48:15-19, 2006

Michael, S., Density functional methods in chemistry and materials science, John Wiley & Sons, 1994

Miyamoto, G., Oh, J. C., Hono, K., Furuhara, T., Make, T., Effect of partitioning of Mn and Si on the growth kinetics of cementite in tempered Fe-0.6 mass% C martensite, *Acta Materialia*, 55:5027-5038, 2007

Monkhorst, H. J., Pack, J. D., Special points for Brillouin-zone integrations, *Physical Review B*, 13:5188-5192, 1976

Owen, W. S., The effect of silicon on the kinetics of tempering, *Trans. ASM*, 46:812-829, 1954

Perdew, J. P., Burke, K., Ernzerhof, M., Generalized gradient approximation made simple, *Physical Review Letters*, 77:3865-3868, 1996

Pollack, *Materials Science and Metallurgy*, 4th ed. Prentice-Hall, 1988

Pomey, J., Revenu de la martensite et reaction bainitique inferieure – cas des aciers au carbone-sliicium et des aciers au carbone, *Memorires Scientifiques Rev. Metallurg.*, 63:507-532, 1966

Rath, J, Freeman, A. J., Generalized magnetic susceptibilities in metals, application of the analytic tetrahedron linear energy method to Sc, *Physical Review B*, 11:2109-2117, 1975

Sakurai, J. J., Modern Quantum Mechanics, Addison Wesley Longman, 1994

Sandvik, B. J. P., The bainite reaction in Fe-Si-C alloys, the primary stage, *Metallurgical Transactions*, 13A:777-787, 1982

Sandvik, B. J. P., The bainite reaction in Fe-Si-C alloys, the secondary stage, *Metallurgical Transactions A*, 13A:789-800, 1982

Speer, J. G., Edmonds, D. V., Rizzo, F. C., Matlock, D. K., Partitioning of carbon from supersaturated plates of ferrite, with application to steel processing and fundamentals of the bainite transformation, *Current Opinion in Solid State and Materials Science*, 8:219-237, 2004

Tsuzuki, A., Sago, S., Hirano, S. I., Naka, S., High temperature and pressure preparation and properties of iron carbides Fe_7C_3 and Fe_3C, *Journal of Materials Science*, 19:2513-2518, 1984

Weinert, M., Kim, I. G., Song, J. H., Freeman, A. J., Unpublished work, 2008

Weinert, M., Wimmer, E., and Freeman, A. J., Total-energy all-electron density functional method for bulk solids and surfaces, *Physical Review B*, 26:4571-4578, 1982

Wimmer, E., Krakauer, H., Weinert, M., Freeman, A. J., Full potential self-consistent linearized augmented plane-wave method for calculating the electronic structure of molecules and surfaces: O_2 molecule, *Physical Review B*, 24:864-875, 1981

Wood, I. G., Cadlo, L. V., Knight, K. S., Dobson, D. P., Marshall, W. G., Price, G. D., Brodholt, J., Thermal expansion and crystal structure of cementite, Fe_3C, between 4 and 600 K determined by time-of-flight neutron powder diffraction, *Journal of Applied Crystallography*, 37:82-90, 2004

Yang, Z. G., Fang, H. S., An overview on bainite formation in steels, *Current Opinion in Solid State and Materials Science*, 9:277-286, 2005

Appedix

This is the documentation for the new database of cementite for MTDATA.

```
Fe:C<cementite:3:1>        E/J        T/K        P/Pa
*** G-HSER(T,P) DATA FORMAT ***
298.150              0.000     1          tcfe
3
-15.7450000E+03              7.06040000E+02              -1.20600000E+02
6000.000
0
6
2.63852850E-05
2.40652500E-05
2.06925000E-08
0.0000000
0.0000000
6.5280750

Si:C<cementite:3:1>        E/J        T/K        P/Pa
*** G-HSER(T,P) DATA FORMAT ***
298.150              0.000     1          tcfe
3
235.7450000E+03              7.06040000E+02              -1.20600000E+02
6000.000
0
6
2.63852850E-05
2.40652500E-05
2.06925000E-08
0.0000000
0.0000000
6.5280750

Si,Fe:C<cementite:3:1>     E/J
*** GEX(REDLICH-KISTER) DATASET FORMAT ***
298.150              1
2
-134.92600000000E+03      0
6000.000
0 0

Al:C<cementite:3:1>        E/J        T/K        P/Pa
```

```
*** G-HSER(T,P) DATA FORMAT ***
298.150              0.000     1          tcfe
3
62.7450000E+03               7.06040000E+02   -1.20600000E+02
6000.000
0
6
2.63852850E-05
2.40652500E-05
2.06925000E-08
0.0000000
0.0000000
6.5280750

Al,Fe:C<cementite:3:1>    E/J
*** GEX(REDLICH-KISTER) DATASET FORMAT ***
298.150              1
2
-127.92600000000E+03      0
6000.000
0 0

Mn:C<cementite:3:1>       E/J        T/K        P/Pa
*** G-HSER(T,P) DATA FORMAT ***
298.150              0.000     1          tcfe
3
-66.7450000E+03              7.06040000E+02              -1.20600000E+02
6000.000
0
6
2.63852850E-05
2.40652500E-05
2.06925000E-08
0.0000000
0.0000000
6.5280750

Mn,Fe:C<cementite:3:1>   E/J
*** GEX(REDLICH-KISTER) DATASET FORMAT ***
298.150  1
2
64.92600000000E+03       0
6000.000
0          0
```

Acknowledgements

I would like to express my sincerely thanks to my supervisor, Professor Bhadeshia, H. K. D. H. who showed me the beauty of science and the fundamental attitude to be a researcher. I am also grateful to Professor Rongshan Qin, Professor Weijie Liu and Professor Pedro Rivera for their so much advice, support and friendship.

나이 서른이 넘도록 집에서 투정부리는 철없는 막내아들 받아주시는 어머니와 아버지께 감사 드립니다. 축구와 초밥, 대게를 좋아하는 우리 형과 호주에서 열심히 살고 있을 우리 누나, 그리고 컴퓨터 게임 못하게 해서 삐쳐 있는 동생 성현이에게 감사합니다.

재료공학에 대해 아무것도 모르던 제게 철강대학원에서 공부할 수 있는 기회와 가르침을 주신 지도교수님 김인기 교수님과 철강대학원 이해건 원장님께 감사 드립니다. 수업을 통해 새로운 지식과 더불어 연구자로써의 열정을 가르쳐 주신 이병주 교수님께 감사 드립니다. 아직 많이 부족한 제게 포스코 입사할 기회를 주시고 신경 써 주신 이재곤 박사님께 감사 드립니다.

떡뽁이 사먹을 돈 없을 때 떡뽁이랑 튀김 사준, 앞으로도 사줄 분식 동호회 지현이에게 감사합니다. 매일 오후 세시 졸음을 깨워주는 다과동호회 재용과 준학, 용기에게 감사합니다. 저녁시간의 무료함을 달래주는 영국식 스포츠동호회 대우와 홍석, 주현에게 감사합니다. 연구를 진행함에 있어 지원을 아끼지 않는 철강대학원 행정 팀 미녀 선생님들, 제니스와 영지 선생님, 예진 선생님, 민정 선생님께 감사 드립니다. 늘 웃는 모습으로 인사 받아주시며 연구실과 건물 깨끗하게 유지해 주시는 아주머니에게 감사 드립니다. 병특기간 동안 JCE 에서 만난 인연으로 각각 일본, 미국에서 같은 분야 공부하며 많은 도움 주고 있는 아이스베리 멤버 학성과 동응에게 감사합니다. 프로그래머에게 필요한 지식과 끊임없는 자기개발 필요성 가르쳐 주신, 지금은 JCE의 임원이 되어 있을 프리스타일 팀 송팀장님과 지현 누님께 감사 드립니다. 마지막으로 지금 각자 자기 분야에서 최고 열심히 노력하며 살고 있을 수학과 98학번 동기들과 철강대학원의 모든 교수님들과 학생들, 연구원들께 감사 드립니다.

CURRICULUM VITAE

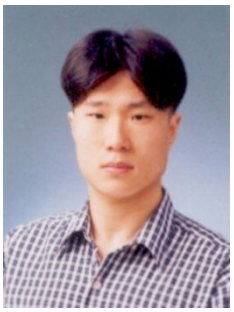

Name: Jang, Jae Hoon (張在勳)

Date of birth: 16th January, 1980

Place of birth: Pohang-Si, South Korea

Address: SK View apt. 109-401
Hyoja-Dong, Nam-Gu, Pohang,
Kyungbuk, 790-784, South Korea

Education:

M. S. 2009, POSTECH (Pohang, Korea), Graduate Institute of Ferrous Technology, Computational Metallurgy.

B. S. 2007, POSTECH (Pohang, Korea), Department of Mathematics / Computer Science and Engineering

Publications

Jang, J. H., Kim, I. G. and Bhadeshia, H. K. D. H., Substitutional solution of silicon in cementite: A first-principles study, *Computational Materials Science*, doi:10.1016/j.commatsci.2008.08.022, 2008

Pak, J. H., Jang, J. H., Bhadeshia, H. K. D. H., and Karlsson, L., Optimization of Neural Network for Charpy Toughness of Steel Welds, *Materials and Manufacturing Processes*, doi:10.10800/10426910802540232, 2009